

Precise control of microtubule disassembly in living cells

Grace Y Liu^{1,†}, Shiao-Chi Chen^{1,†}, Gang-Hui Lee^{2,3,†}, Kritika Shaiv¹, Pin-Yu Chen¹, Hsuan Cheng¹, Shi-Rong Hong¹, Wen-Ting Yang¹ , Shih-Han Huang¹, Ya-Chu Chang¹, Hsien-Chu Wang¹, Ching-Lin Kao¹, Pin-Chiao Sun¹, Ming-Hong Chao¹, Yian-Ying Lee¹, Ming-Jer Tang^{2,3}  & Yu-Chun Lin^{1,4,*} 

Abstract

Microtubules tightly regulate various cellular activities. Our understanding of microtubules is largely based on experiments using microtubule-targeting agents, which, however, are insufficient to dissect the dynamic mechanisms of specific microtubule populations, due to their slow effects on the entire pool of microtubules. To overcome this technological limitation, we have used chemo and optogenetics to disassemble specific microtubule subtypes, including tyrosinated microtubules, primary cilia, mitotic spindles, and intercellular bridges, by rapidly recruiting engineered microtubule-cleaving enzymes onto target microtubules in a reversible manner. Using this approach, we show that acute microtubule disassembly swiftly halts vesicular trafficking and lysosomal dynamics. It also immediately triggers Golgi and ER reorganization and slows the fusion/fission of mitochondria without affecting mitochondrial membrane potential. In addition, cell rigidity is increased after microtubule disruption owing to increased contractile stress fibers. Microtubule disruption furthermore prevents cell division, but does not cause cell death during interphase. Overall, the reported tools facilitate detailed analysis of how microtubules precisely regulate cellular architecture and functions.

Keywords intercellular bridge; microtubule; mitotic spindle; primary cilium; spastin

Subject Categories Methods & Resources; Organelles

DOI 10.15252/embj.2021110472 | Received 22 December 2021 | Revised 15 April 2022 | Accepted 5 May 2022 | Published online 10 June 2022

The EMBO Journal (2022) 41: e110472

Introduction

Microtubules are hollow tubes constructed from α - and β -tubulins and are present in all eukaryotic cells. They are involved in many

cellular activities including intracellular trafficking, cell migration, cell division, cell polarity, signaling and others (Janke & Magiera, 2020; Cleary & Hancock, 2021). Different microtubule subpopulations undergo distinct post-translational modifications (PTMs), which modulate their properties and functions (Janke & Magiera, 2020). Moreover, cells form several microtubule-based structures spatiotemporally such as primary cilia on the surface of G0 cells, intercellular bridges in the connected regions of two dividing cells during telophase, mitotic spindles in the cytosol of metaphase cells, and centrosomes in the perinuclear region or cell cortex to execute corresponding activities (Doxsey *et al.*, 2005; Prosser & Pelletier, 2017; Antanavičiūtė *et al.*, 2018; Yang *et al.*, 2021). Defects in these microtubules and relative structures lead to a variety of human diseases including birth defects, neurodegenerative diseases, ciliopathies, and several tumors, highlighting their essential roles (Hildebrandt *et al.*, 2011; Parker *et al.*, 2014; Sferra *et al.*, 2020).

Our understanding of microtubules and these microtubule-based organelles is largely dependent on microtubule-targeting agents (MTAs) that perturb the monomer-polymer tubulin equilibrium and microtubule dynamics (Steinmetz & Prota, 2018). As microtubules are vital for cellular physiology and mitosis, these MTAs have also been used in cancer chemotherapy (Rovini *et al.*, 2011). However, MTAs slowly disrupt microtubule structures, especially for long-lived microtubules such as acetylated microtubules (LeDizet & Piperno, 1986; Friedman *et al.*, 2010; Xie *et al.*, 2010; Xu *et al.*, 2017). Moreover, off-target effects of MTAs have been reported. For instance, nocodazole, a widely used MTA, dramatically inhibits T-cell antigen receptor signaling and insulin-stimulated glucose transport, neither of which is dependent on the ability of nocodazole to depolymerize microtubules (Huby *et al.*, 1998; Molero *et al.*, 2001). These drawbacks make it challenging to dissect the dynamic mechanisms of microtubules and to clearly distinguish microtubule-dependent and microtubule-independent events. The slow disruption of microtubules and off-target effects of MTAs also lead to unexpected side effects in clinical applications (Bates & Eastman, 2017).

1 Institute of Molecular Medicine, National Tsing Hua University, Hsinchu, Taiwan

2 Department of Physiology, College of Medicine, National Cheng Kung University, Tainan, Taiwan

3 International Center for Wound Repair and Regeneration, National Cheng Kung University, Tainan, Taiwan

4 Department of Medical Science, National Tsing Hua University, Hsinchu, Taiwan

*Corresponding author. Tel: +886 3 5742421; E-mail: ycl@life.nthu.edu.tw

[†]These authors contributed equally to this work

Recently, many efforts have been made to precisely control the dynamics and behavior of targeted microtubule subtypes. Van Haren *et al* (2018) developed an optogenetic tool to spatiotemporally disassociate a plus-end-tracking protein, EB1, from microtubules, which attenuates microtubule growth as well as cell migration. Adikes *et al* (2018) used light illumination to modulate the cross-link between microtubule plus ends and actin filaments. Moreover, a photoswitchable MTA was developed to reversibly modulate microtubule dynamics in light-illuminated cells (Borowiak *et al*, 2015). These tools have raised the possibility of spatiotemporally controlling microtubule activities. However, none of these systems can directly disassemble specific microtubule subtypes and microtubule-based structures. To overcome these long-standing issues, we have developed a new and easy-to-use system that enables precise disassembly of targeted microtubule subtypes or several microtubule-based structures including tyrosinated microtubules, primary cilia, mitotic spindles, and intercellular bridges under the control of chemical treatments or light illumination. With the ability to disrupt microtubule subtypes with spatial and temporal accuracy, we have comprehensively characterized the direct roles that microtubules have in cellular architecture and activities.

Results

Rapid translocation of proteins of interest onto microtubules

The chemically inducible dimerization (CID) system has been used to manipulate cellular signaling and molecular composition over both space and time (DeRose *et al*, 2013; Fan *et al*, 2017; Hong *et al*, 2018). This is achieved by the rapid recruitment of proteins of interest (POIs) onto specific subcellular sites or their substrates (DeRose *et al*, 2013). Dimerization of FKBP (FK506-binding protein) and FRB (FKBP-rapamycin binding domain) that is triggered by a small chemical component, rapamycin, is one well-established CID system (DeRose *et al*, 2013). To rapidly recruit POIs onto microtubules, we tagged FRB with a microtubule-binding sequence, EMTB (the microtubule-binding domain of ensconsin), and a cyan fluorescent protein (CFP) for visualizing its distribution (Fig 1A and B). A linescan analysis showed that the resulting construct, EMTB-CFP-FRB, colocalizes with cytosolic microtubules labeled by an antibody against α -tubulin (Appendix Fig S1). The addition of rapamycin to HeLa cells led to the rapid translocation of yellow fluorescent protein-tagged FKBP (YFP-FKBP) onto EMTB-CFP-FRB-labeled microtubules as evidenced by an increased FRET (fluorescence resonance energy transfer) signal on microtubules ($T_{1/2}$ of translocation: 5.73 ± 0.54 s; Fig 1B and C, Movie EV1). In summary, these results demonstrated that cytosolic POIs can be rapidly translocated onto microtubules through inducible protein dimerization.

Engineering microtubule-severing enzymes for precise microtubule disruption

Spastin is a microtubule-severing enzyme that is ubiquitous in nearly all eukaryotic cells (Rodrigues & Ballesteros, 2007). Consistent with a previous study (Lacroix *et al*, 2010), expression of full-length spastin (Spastin-YFP) and truncated spastin without the N-terminal 1–140 amino acids (dNSpastin-YFP) in HeLa cells

removed significant amounts of cytosolic microtubules, 47.45 and 42.86%, respectively, relative to YFP-transfected control cells (Fig EV1A and C). Thus, the N-terminal fragment (1–140 amino acids) was dispensable for Spastin-mediated microtubule severing. To minimize the microtubule-cleaving reaction before recruitment of Spastins onto microtubules, we next attempted to disassociate dNSpastin from microtubules by three strategies and also tagged Spastin with YFP-FKBP: (i) removal of the microtubule-binding domain from dNSpastin while retaining its catalytic domain (dNSpastinCD-YFP-FKBP); (ii) mutation of key residues that are required for microtubule binding of Spastin (dNSpastin3Q-YFP-FKBP) (Eckert *et al*, 2012); and (iii) tagging Spastin with a plasma membrane-binding sequence, C2Lact (Fan *et al*, 2017), to mislocate Spastin to the cell cortex, where microtubules are rarely found (dNSpastin-YFP-FKBP-C2Lact). We then characterized the enzyme activities of the above constructs before and after they were recruited onto microtubules. dNSpastin-YFP-FKBP-C2Lact and dNSpastin3Q-YFP-FKBP showed low microtubule-severing activities before rapamycin treatment and robustly disrupted microtubules after rapamycin treatment (Fig EV1B and C). dNSpastinCD-YFP-FKBP did not show severing activity, which is consistent with a previous report, suggesting other domains of spastin may also be important to perform microtubule severing (Fig EV1B and C; White *et al*, 2007). Live-cell imaging revealed that rapamycin treatment rapidly triggered the translocation of dNSpastin-YFP-FKBP-C2Lact ($T_{1/2} = 55.44 \pm 8.38$ s) and dNSpastin3Q-YFP-FKBP ($T_{1/2} = 60.35 \pm 5.30$ s) from the cytosol onto microtubules (Appendix Fig S2 and Movie EV2). It was noteworthy that microtubule disruption triggered by dNSpastin3Q-YFP-FKBP upon rapamycin treatment ($T_{1/2} = 11.05 \pm 1.52$ min) was much faster than that of dNSpastin-YFP-FKBP-C2Lact upon rapamycin treatment ($T_{1/2} = 53.08 \pm 8.08$ min), and treatment of two common MTAs, nocodazole (3.3 μ M; $T_{1/2} = 106.86 \pm 14.20$ min) and colchicine (500 μ M; $T_{1/2} = 94.28 \pm 8.63$ min; Appendix Fig S3A and B, Movies EV3 and EV4). Moreover, recruitment of dNSpastin3Q-YFP-FKBP onto microtubules significantly removed more microtubule filaments as compared to other treatments (Appendix Fig S3C). The acetylated microtubules are long-lived microtubules, which resist nocodazole treatment, but can be removed immediately and completely after recruitment of dNSpastin3Q onto microtubules (Fig 1F and G). Trapping the enzyme-inactive dNSpastin3QED-YFP-FKBP onto microtubules showed no microtubule disruption, indicating that acute microtubule disruption is an enzyme-dependent event (Appendix Fig S3A and C, and Movie EV4). This inducible microtubule disruption occurs in other cell types (Appendix Figs S4 and S5, Movies EV5 and EV6) and can also be controlled by rapamycin-orthogonal systems such as a gibberellin-based system with similar microtubule disruption kinetics (Appendix Figs S6 and S7, Movie EV7; Fan *et al*, 2017). Moreover, dNSpastin3Q-mediated microtubule disruption did not result in a change in the amount of microtubule mass as well as microtubule disruption rate when cells were pretreated with the proteasome inhibitor MG132, indicating that this event was not dependent on proteasome-mediated degradation (Fig 1E, Appendix Figs S3B and C, and S8, Movie EV8). Moreover, spastazoline, a Spastin inhibitor (Cupido *et al*, 2019), swiftly reversed rapamycin-mediated acute microtubule disruption (Fig EV2A and B, Movie EV9). Intriguingly, nascent microtubules from the fragments derived from dNSpastin3Q-mediated cleavage

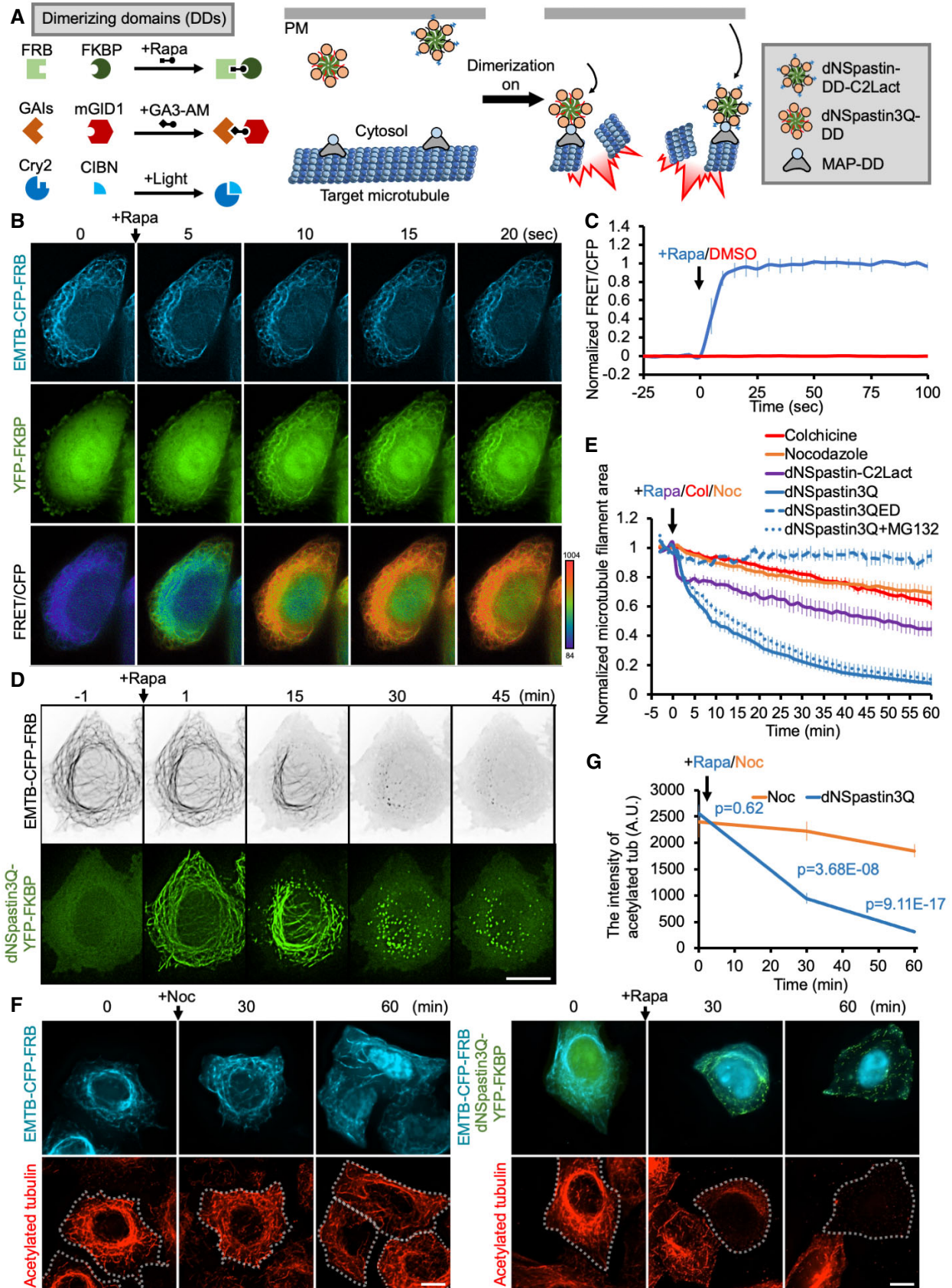


Figure 1.

Figure 1. Recruitment of engineered Spastins onto microtubules leads to their rapid disassembly.

- A Schematic of the inducible microtubule disassembly system. Dimerization of three different pairs FRB/FKBP, GAls/mGID1, and Cry2/CIBN can be triggered by rapamycin (Rapa), GA3-AM, and blue light, respectively. One of the dimerizing domains (DDs) is fused with one of two engineered Spastin enzymes, dNSpstin3Q and C2Lact-tagged dNSpstin, whereas the other is fused with microtubule-associated proteins (MAPs). Dimerization upon certain stimuli (e.g., chemical treatments or light illumination) induces recruitment of engineered Spastins from cytosol or plasma membrane (PM) onto MAP-labeled microtubules. Acute accumulation of Spastins on microtubules rapidly induces disassembly of target microtubules.
- B HeLa cells co-transfected with EMTB-CFP-FRB and YFP-FKBP were treated with 100 nM rapamycin (Rapa). Addition of rapamycin rapidly translocated YFP-FKBP onto EMTB-CFP-FRB-labeled microtubules and increased the FRET signal. The scale for the FRET/CFP intensity ratio is shown. Scale bar, 10 μ m.
- C The normalized intensity of FRET/CFP in cells before and after rapamycin (blue) and 0.1% DMSO (control; red) treatment. $n = 6$ and 10 cells in the rapamycin and DMSO groups, respectively, from three independent experiments. Data are shown as the mean \pm SEM.
- D The video frames of microtubule disruption upon the recruitment of dNSpstin3Q-YFP-FKBP onto microtubules. HeLa cells co-transfected with the indicated constructs were treated with rapamycin (100 nM). Scale bar, 10 μ m.
- E The normalized microtubule filament area in cells with different microtubule disruption treatments. $n = 30, 45, 19, 20, 14,$ and 6 cells in nocodazole (3.3 μ M), colchicine (500 μ M), dNSpstin-YFP-FKBP-C2Lact, dNSpstin3Q-YFP-FKBP, dNSpstin3QED-YFP-FKBP, and dNSpstin3Q-YFP-FKBP with MG132 (50 μ M) pre-treatment, respectively, from three independent experiments. Data are shown as the mean \pm SEM.
- F HeLa cells co-transfected with the indicated constructs were treated with nocodazole (Noc, 3.3 μ M; left) or rapamycin (Rapa, 100 nM; right) for 0, 30, and 60 min. Transfected cells were then fixed and labeled with anti-acetylated tubulin (red). Dotted lines indicate the boundary of transfected cells. Scale bars, 10 μ m.
- G The intensity of acetylated tubulin in cells transfected with EMTB-CFP-FRB (orange) or co-transfected with EMTB-CFP-FRB and dNSpstin3Q-YFP-FKBP (blue) after the addition of nocodazole (Noc, 3.3 μ M) or rapamycin (Rapa, 100 nM) for the indicated times. $n = 123$ and 81 cells in the nocodazole and dNSpstin3Q groups, respectively, from three independent experiments. Data are shown as the mean \pm SEM. Student's *t*-tests were performed, with *P*-values indicated.

assembled at a polymerization rate of $0.92 \pm 0.04 \mu\text{m/s}$, which was slightly slower than the regrowth rate of $1.17 \pm 0.07 \mu\text{m/s}$ for microtubules from centrosomes (Fig EV2C). Taken together, these results demonstrate that acute microtubule disruption occurs through microtubule filament disassembly instead of microtubule degradation. In summary, rapid recruitment of dNSpstin3Q-YFP-FKBP onto microtubules efficiently triggers microtubule disassembly in living cells upon dimerization induction.

Rapid disruption of specific microtubule-based structures

Many microtubule-based structures including primary cilia, centrosomes, mitotic spindles, and intercellular bridges regulate various cellular activities in a defined spatiotemporal manner (Doxsey *et al*, 2005; Prosser & Pelletier, 2017; Antanavičiūtė *et al*, 2018; Yang *et al*, 2021). We next tested whether the recruitment of dNSpstin3Q onto these different microtubule-based structures can specifically disassemble them. A truncated microtubule-binding domain of microtubule associate protein 4 (MAP4m) preferentially binds to ciliary axonemes in G0 cells and shifts to mitotic spindles during metaphase and intercellular bridges during telophase (Appendix Fig S9; Hong *et al*, 2018). In G0 cells, addition of rapamycin rapidly trapped FKBP-tagged dNSpstin3Q on CFP-FRB-MAP4m-labeled

axonemes in the cilia. Local accumulation of dNSpstin3Q on ciliary axonemes resulted in rapid disassembly of axonemes and primary cilia within ~ 15 min (Fig 2A and B, Appendix Fig S10, Movie EV10). Trapping enzyme-inactive dNSpstin3QED-YFP-FKBP on ciliary axonemes did not perturb the ciliary structure (Appendix Fig S10 and Movie EV10). Although axonemes are known as major skeletons of primary cilia, acute axoneme disruption was occasionally not associated with disassembly of the entire ciliary structure (2 out of 10 cells examined) and induced bulging and branched phenotypes in cilia (Appendix Fig S11 and Movie EV11), suggesting that other microtubule-independent factors may also contribute to the maintenance of ciliary structures. This may explain why long cilia still maintain their structure without fully extended axonemes in proximal end. In mitotic cells, translocation of dNSpstin3Q onto CFP-FRB-MAP4m-labeled mitotic spindles (Fig 2C) and intercellular bridges (Fig 2E) quickly disrupted these microtubule-based structures (Fig 2C–F, Movies EV12 and EV13). Surprisingly, dNSpstin3Q cannot rapidly disrupt centrosomes (or basal bodies in G0 cells) as shown by the images of cells that retained PACT (a conserved centrosomal-targeting motif of pericentrin protein) (Gillingham & Munro, 2000)-labeled centrosomes after microtubule disruption treatment for 1 h (Appendix Fig S12 and Movie EV14).

Figure 2. Rapid disruption of primary cilia, mitotic spindles, and intercellular bridges.

- A NIH3T3 fibroblasts co-transfected with 5HT6-mCherry (5HT6-mCh; a ciliary membrane marker; red), CFP-FRB-MAP4m (blue), and dNSpstin3Q-YFP-FKBP (green) were serum-starved for 24 h to induce ciliogenesis. Ciliated cells were then treated with rapamycin (Rapa, 100 nM) to induce dNSpstin3Q-YFP-FKBP recruitment to axonemal microtubules. Dotted lines indicate the cell boundaries. Scale bar, 5 μ m.
- B The normalized length of axonemes (blue), primary cilia (red), and dNSpstin3Q-YFP-FKBP in cilia (green) upon rapamycin treatment. $n = 6$ cells from three independent experiments. Data are shown as the mean \pm SEM.
- C HeLa cells co-transfected with H2B-mCherry (H2B-mCh; a chromosome marker; red), CFP-FRB-MAP4m (a marker of mitotic spindles; blue), and dNSpstin3Q-YFP-FKBP (green) were synchronized in metaphase and treated with rapamycin (100 nM) to induce dNSpstin3Q-YFP-FKBP recruitment to mitotic spindles. Dotted lines indicate the cell boundaries. Scale bar, 10 μ m.
- D The normalized area of the mitotic spindle (blue) and intensity of dNSpstin3Q-YFP-FKBP in the mitotic spindle (green) upon rapamycin treatment. $n = 6$ cells from three independent experiments. Data are shown as the mean \pm SEM.
- E HeLa cells co-transfected with H2B-mCherry (red), CFP-FRB-MAP4m (intercellular bridges; blue), and dNSpstin3Q-YFP-FKBP (green) were treated with rapamycin (100 nM) to induce dNSpstin3Q-YFP-FKBP recruitment to intercellular bridges. Arrows indicate the intercellular bridges. Dotted lines indicate the cell boundaries. Scale bar, 10 μ m.
- F The normalized area of intercellular bridges (blue) and intensity of dNSpstin3Q-YFP-FKBP at intercellular bridges (green) upon rapamycin treatment. $n = 5$ cells from three independent experiments. Data are shown as the mean \pm SEM.

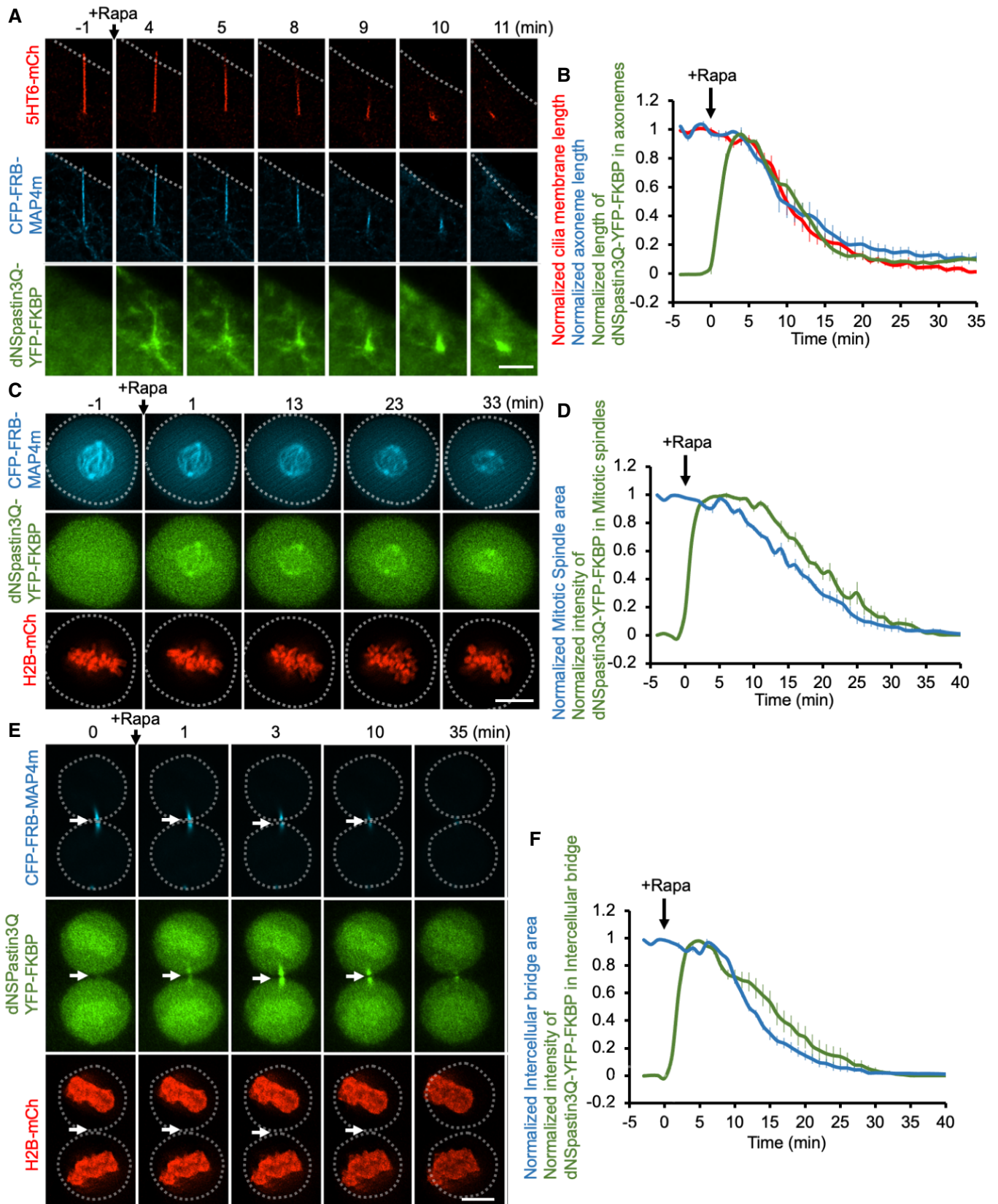


Figure 2.

Rapid disruption of microtubules with different post-translational modifications

Microtubules undergo various PTMs for spatiotemporally regulating their properties and functions (Janke & Magiera, 2020). We next turned our efforts to precisely disrupt microtubules with specific PTMs. Very recently, an elegant work has established a biosensor, A1AY1, which specifically targets highly tyrosinated microtubules in living cells (Kesarwani *et al*, 2020). To apply it in our system, A1AY1 was tagged with FRB and a red fluorescent protein, TagRFP. Immunostaining results confirmed that the regulating construct (TagRFP-FRB-A1AY1) preferentially targeted to generic microtubules and highly tyrosinated microtubules but not to detyrosinated microtubules (Fig 3A–C). The addition of rapamycin rapidly recruited a cyan fluorescent protein, TagCFP, tagged FKBP (TagCFP-FKBP), onto TagRFP-FRB-A1AY1-bound microtubules ($T_{1/2} = 64.71 \pm 16.08$ s; Fig 3D and E and Movie EV15). Moreover, recruitment of dNSpstin3Q-TagCFP-FKBP onto A1AY1-labeled microtubules disrupted the A1AY1-positive microtubule filaments and significantly reduce ~41.4% of tyrosinated microtubules within 1 h (Fig 3F and G), indicating that, with specific tubulin PTMs biosensor against highly tyrosinated microtubules, our system is able to reduce the level of highly tyrosinated microtubules. Since the tyrosinated microtubules are abundant in growth cones of neuronal axons (Janke & Magiera, 2020), our system serves as a promising tool to disturb tyrosinated microtubule level and uncover its roles in neuronal structure and functions.

We next tested the disruption efficiency on different modified microtubules. Overexpression of a detyrosination protein complex, VASH1 (vasohibin 1)/SVBP (small vasohibin binding protein) complex (Aillaud *et al*, 2017), and a truncated glutamylase, TLL4C639 (the C639 fragment of TLL4) (van Dijk *et al*, 2007), significantly increased the level of detyrosinated and glutamylated microtubules, respectively (Fig EV3A–D). EMTB-CFP-FRB efficiently bound to unmodified, detyrosinated, and glutamylated microtubules in YFP alone, VASH1-YFP/SVBP, and TLL4C639-YFP-transfected cells, respectively. We, therefore, used EMTB-CFP-FRB to recruit dNSpstin3Q-mCh-FKBP onto unmodified and modified microtubules and compared their severing activities (Fig EV3E). Intriguingly, disruption of glutamylated microtubules was slower than that of unmodified microtubules (Fig EV3E–G and Movie EV16). There was no significant difference in microtubule disruption rates between

detyrosinated and unmodified microtubules (Fig EV3E–G and Movie EV16). These data indicate the glutamylation but not detyrosination slows down the Spastin-mediated microtubule severing.

Using light to spatiotemporally disrupt microtubules

Rapamycin-inducible dimerization has been widely considered as an irreversible process as the clearance of rapamycin from cells is very slow (~30 h) due to extremely high affinity between rapamycin and FKBP (Putyrski & Schultz, 2012; Lin *et al*, 2013; Voß *et al*, 2015). To control microtubule disruption with better spatiotemporal precision, we next tried to use an optogenetic system to trigger microtubule disassembly in a subcellular region of interest during a specific period of time. Cryptochrome 2 (Cry2) and CIBN (consisting of the N-terminal 1–81 amino acids of CIB1), two blue light-sensitive dimerizing partners (Taslimi *et al*, 2016), were used in our microtubule-manipulating system. Cry2, which was tagged with the red fluorescent protein mCherry (mCh-Cry2), was rapidly translocated onto EMTB-YFP-CIBN-labeled microtubules only in regions illuminated with light ($T_{1/2} = 34.6 \pm 7.58$ s) and dissociated from microtubules to the cytosol when the light was off ($T_{1/2} = 28.2 \pm 4.88$ s; Fig 4A and B, and Movie EV17). We then used light to control Spastin-mediated microtubule disassembly in a spatially and temporally specific manner. dNSpstin3Q tagged with mCh-Cry2 was co-expressed with EMTB-YFP-CIBN in COS7 cells. Microtubules were labeled with SPY650-tubulin in these experiments. Local illumination with blue light robustly recruited dNSpstin3Q-mCh-Cry2 onto microtubules, leading to the disassembly of microtubules only in illuminated regions. The dNSpstin3Q-mCh-Cry2 reverted to cytosol and microtubule reassembly occurred when the cells were placed back in the dark (Fig 4C and D, Movie EV18). Recruitment of mCh-Cry2 without Spastin onto microtubules by the same photostimulation procedure did not lead to microtubule disassembly, confirming that light-induced microtubule disassembly does not result from phototoxicity (Appendix Fig S13 and Movie EV19).

Acute microtubule disassembly inhibits vesicular trafficking and lysosomal dynamics

The roles of microtubules in vesicular trafficking and organelle dynamics have been well studied using MTAs (Schuh, 2011; Ba

Figure 3. Disruption of tyrosinated microtubules.

- A COS7 cells transfected with TagRFP-FRB-A1AY1 (red) were labeled by anti- α -tubulin antibody (green; upper panel), anti-tyrosinated tubulin antibody (green; middle panel), or anti-detyrosinated tubulin antibody (green; lower panel), respectively. Scale bar, 10 μ m.
- B The intensity profiles of TagRFP-FRB-A1AY1 (red) and tubulin with the indicated PTMs (green) along dotted lines drawn in (A).
- C The Pearson's correlation coefficients for TagRFP-FRB-A1AY1 and indicated tubulin (tub) subtypes were calculated, and data are shown as the mean \pm SEM. $n = 16$, 13, and 15 cells from left to right, respectively; three independent experiments.
- D COS7 cells co-transfected with TagRFP-FRB-A1AY1 (red) and TagCFP-FKBP (green) were treated with rapamycin (100 nM). The addition of rapamycin rapidly recruits TagCFP-FKBP from cytosol onto A1AY1-labeled microtubules (arrows). Scale bar, 10 μ m.
- E The normalized intensity of TagCFP-FKBP at A1AY1-labeled microtubules upon rapamycin treatments. $n = 7$ cells from three independent experiments. Data are shown as the mean \pm SEM.
- F COS7 cells co-transfected with TagRFP-FRB-A1AY1 (red) and dNSpstin3Q-TagCFP-FKBP (cyan) were treated with 0.1% DMSO or rapamycin (100 nM) for 1 h and followed by immunostaining with anti-tyrosinated tubulin antibody (green). Dotted lines highlight the transfected cells. Scale bar, 20 μ m.
- G The normalized intensity of tyrosinated microtubules in TagRFP-FRB-A1AY1 and dNSpstin3Q-TagCFP-FKBP co-transfected cells upon 0.1% DMSO or rapamycin treatment for 1 h. $n = 31$ and 26 cells in DMSO and rapamycin-treated groups, respectively, from three independent experiments. Data (blue) represent as mean \pm SEM. Student's *t*-tests were performed with *P*-values indicated.

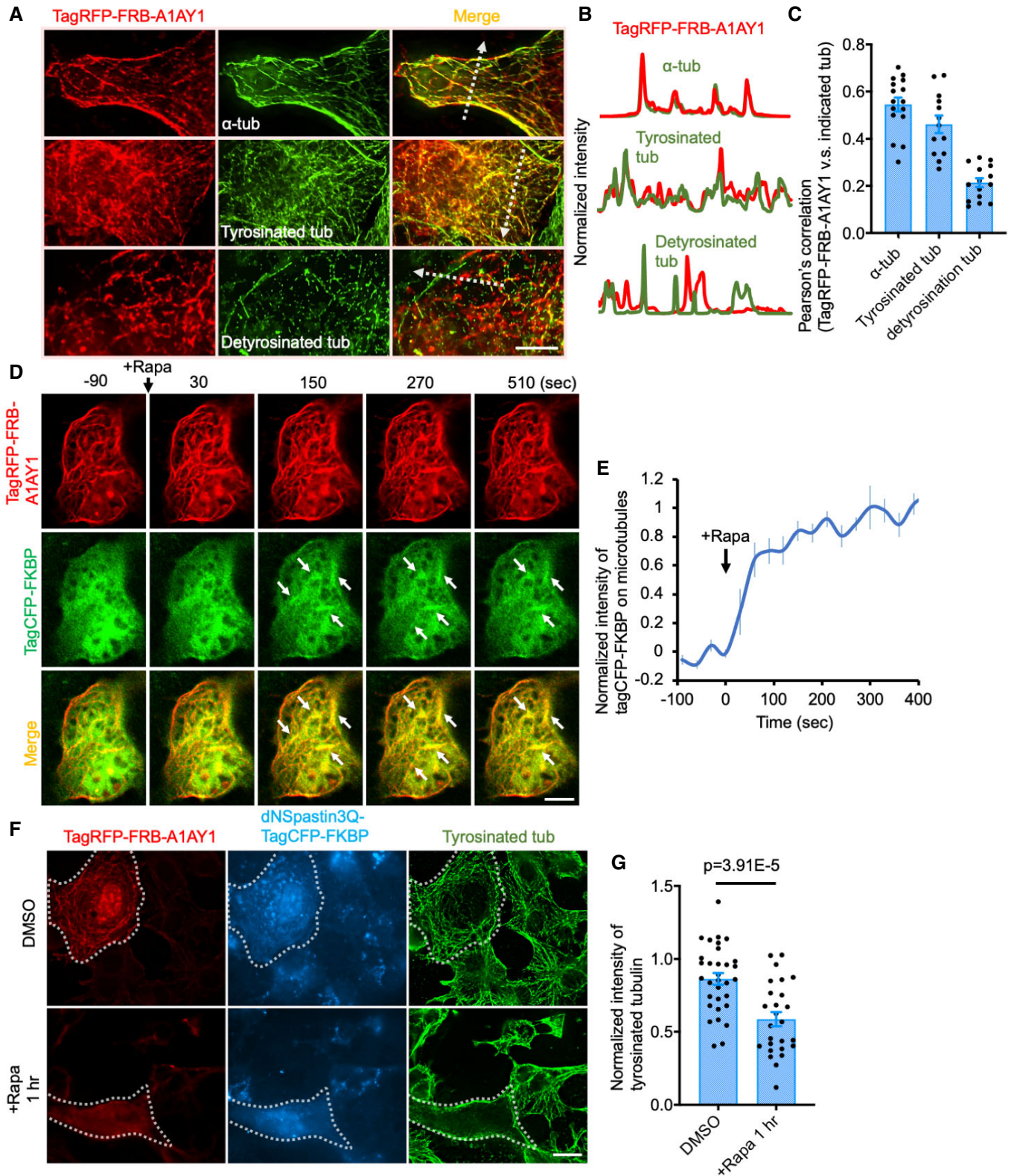


Figure 3.

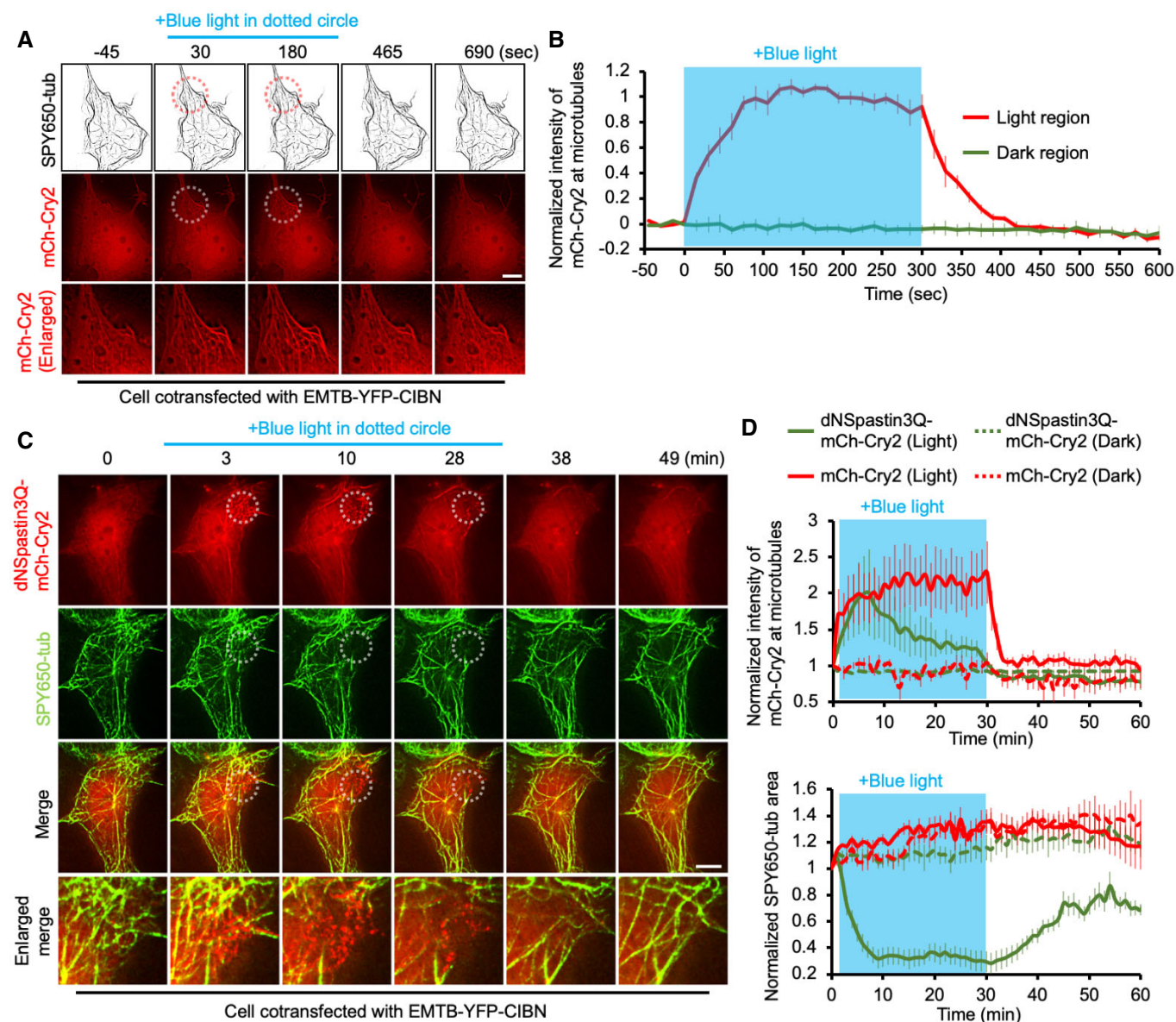


Figure 4. Using light to disassemble microtubules in a reversible and location-specific manner.

- A** COS7 cells co-transfected with EMTB-YFP-CIBN and mCh-Cry2 (red) were incubated with SPY650-tubulin (SPY650-tub) to visualize microtubules. The cells were illuminated by blue light within a specified region (indicated by the dotted circle) for the indicated time period. Scale bar, 10 μ m.
- B** The normalized intensity of mCh-Cry2 at microtubules in illuminated regions (red) and non-illuminated regions (green). $n = 6$ cells from three independent experiments. Data are shown as the mean \pm SEM.
- C** COS7 cells co-transfected with EMTB-YFP-CIBN and dNSpstin3Q-mCh-Cry2 were incubated with SPY650-tubulin to visualize microtubules. The cells were illuminated by blue light as in (A). Scale bar, 10 μ m.
- D** The normalized intensity of dNSpstin3Q-mCh-Cry2 and mCh-Cry2 at microtubules and the normalized area of SPY650-tubulin in illuminated regions and non-illuminated regions. $n = 6$ and 6 cells in dNSpstin3Q-mCh-Cry2 and mCh-Cry2 groups, respectively, from three independent experiments. Data are shown as the mean \pm SEM.

et al., 2018). However, several long-lived microtubules that are more resistant to MTAs often act as major railways for transporting cargo and regulating organelle organization in cells (Friedman et al., 2010; Noordstra & Akhmanova, 2017; Meiring et al., 2020). Therefore, the interpretations of how microtubules are involved in vesicular trafficking and organelle dynamics in experiments involving MTAs need to be carefully re-examined. Given that our system is sufficient

to completely disassemble almost the entire pool of microtubules, no matter their longevity (Fig 1), we evaluated whether acute microtubule disassembly functionally perturbs vesicle and organelle dynamics. To this end, a YFP-labeled post-Golgi vesicle marker, TGN38 (trans-Golgi network integral membrane protein 38), and a lysosome marker, LAMP3 (lysosome-associated membrane glycoprotein 3), were used to observe the real-time dynamics of vesicles

and lysosomes upon acute microtubule disassembly, respectively (Fig EV4 and Movies EV20–EV23). Moreover, the trajectories of TGN38-YFP and LAMP3-YFP upon microtubule disassembly were analyzed by automated particle detection and tracking algorithms (Fig EV4B and F, Movies EV21 and EV23) (Jaqaman *et al*, 2008). Accordingly, the movement and orientation of the labeled proteins were defined as “confined” (i.e., static), free diffusion (i.e., movement with frequent changes in direction), or “directed” (i.e., movement in a constant direction) (Fig EV4B and F). The population of directed TGN38-YFP and LAMP3-YFP particles became confined particles after microtubule disassembly (Fig EV4B and F). We noticed that many TGN38 and LAMP3 particles were defined as free diffusion during microtubule disruption (microtubule 50%), probably due to their transition from directed movement to a confined state (Fig EV4B and F). Regardless of this transition, microtubule disruption did not obviously change the population of free diffusion particles (Fig EV4B and F). As expected, acute microtubule disruption also linearly attenuated the displacement and velocity of TGN38 and LAMP3 particles (Fig EV4C, D, G and H). In summary, our system not only disrupts microtubule structures but also efficiently halts the directional movement of vesicles and lysosomes along microtubules.

Microtubules are essential for the organization of Golgi, endoplasmic reticulum, and mitochondria

We next evaluated the effects of acute microtubule disassembly on organelle organization. The Golgi apparatus in cells was labeled by YFP-Giantin, which resides in the perinuclear region (Fig EV5A and Movies EV24 and EV25). Consistent with the previous observation using MTAs, acute removal of microtubules in cells immediately triggered Golgi dispersal throughout the cells (Fig EV5A and B, Movie EV24). The recruitment of enzyme-dead Spastin onto microtubules did not affect the distribution of the Golgi apparatus (Fig EV5B and Movie EV25), confirming that microtubules are continuously required for maintaining the perinuclear distribution of the Golgi apparatus.

The endoplasmic reticulum (ER) is the organelle highly associated with microtubules (Terasaki *et al*, 1986; Guo *et al*, 2018). However, discrepant morphologies of the ER after disruption or remodeling of microtubules were observed in early studies (Terasaki *et al*, 1986; Bannai *et al*, 2004; Poteryaev *et al*, 2005; Lu *et al*, 2009; Shibata *et al*, 2009; Schroeder *et al*, 2019). Neon-Cb5 (which consists of 17 residues of the transmembrane domain of rat cytochrome b5) was used to label the ER in living cells. The ER exhibits sheet-like structures in the perinuclear region and exists as a network of ER tubules in the cell periphery (Fig EV5C and Movie EV26). Our results showed that upon acute microtubule disassembly, neighboring ER tubules immediately fused with one another and formed sheet-like structures (Fig EV5C and Movie EV26), indicating that microtubules are key components for preventing the fusion of neighboring ER tubules and therefore maintain ER tubules in cells.

We next evaluated the roles of microtubules in mitochondrial dynamics and activities. Mitochondria are known to fuse with one another (fusion) and to divide into separate mitochondria (fission) constantly. The balance of fusion and fission is critical for the morphology and activities of mitochondria (Westermann, 2010). Even

though microtubules serve as a railway for the long-distance transport of mitochondria (Schwarz, 2013), the evidence regarding whether and how microtubules regulate the fusion and fission of mitochondria is still sparse. We used Tom20-Neon (a transmembrane domain from the protein Tom20, translocase of outer mitochondrial membrane 20) to label the outer membrane of mitochondria (Fig 5A). To avoid the intercellular variations of mitochondrial properties, the local movement of each Tom20-Neon-labeled mitochondrion was quantitatively measured by single-cell analysis before and after acute microtubule disruption. Among the examined cells, 88.89% showed significantly reduced local movement for mitochondria after acute microtubule disruption (Fig 5B). Before microtubule disassembly, mitochondrial fusion and fission occurred frequently (Fig 5A and C, Movie EV27). It is noteworthy that in these same cells after microtubule disruption, adjacent mitochondria were capable of attaching to one another but were not able to trigger the fusion process, as the boundary between two neighboring mitochondria was visible for a relatively longer time as compared with that under control conditions (Fig 5A and Movie EV27). Moreover, less mitochondrial fission was observed in the absence of microtubules (Fig 5C and Movie EV27). Quantification confirmed that acute microtubule disruption robustly suppressed both fusion and fission processes (Fig 5C). However, the fusion-to-fission ratio was not changed by microtubule disruption (Fig 5D), indicating that microtubule disruption perturbed fusion and fission simultaneously and to the same extent. To quantitatively evaluate the effects of microtubule removal on the morphology of mitochondria, the ratio of the long axis to the short axis of each mitochondrion was determined (Fig 5E and Movie EV28). Surprisingly, acute microtubule disassembly did not change the morphology of the mitochondria, perhaps owing to only modest changes in the fusion-to-fission ratio (Fig 5E and F). We also evaluated mitochondrial activities using a mitochondrial membrane potential-sensitive dye, MitoTracker Red. Consistent with previous observations that cells may continuously pump out MitoTracker Red (Murota *et al*, 2016), a gradual decrease in the intensity of MitoTracker Red was shown in control cells (Fig 5H). However, microtubule removal did not affect the mitochondrial membrane potential as compared to untransfected control cells and cells expressing enzyme-dead Spastin (Fig 5G and H, Movie EV29). Taken together, our results demonstrated that microtubules power the local movement of mitochondria and positively regulate both fusion and fission processes. Removal of microtubules did not perturb the balance of fusion and fission or the overall morphology of mitochondria, nor did this affect mitochondrial activities.

It is noteworthy that ER-mitochondria contacts have frequently been observed along with tubular ERs (Csordás *et al*, 2010; Friedman *et al*, 2010; Guo *et al*, 2018). Zheng *et al* (2018) demonstrated that DNA damage promotes ER tubular formation accompanied by an increase in ER-mitochondria contacts. This raises a possibility that mitochondria may preferentially associate with ER tubules rather than ER sheets. Acute microtubule disruption robustly converted ER tubules to ER sheets (Fig EV5C and Movie EV26) and might subsequently reduce ER-mitochondria contacts and suppress mitochondrial dynamics. The interplay between ER and mitochondria upon microtubule disassembly will need to be evaluated to address this hypothesis.

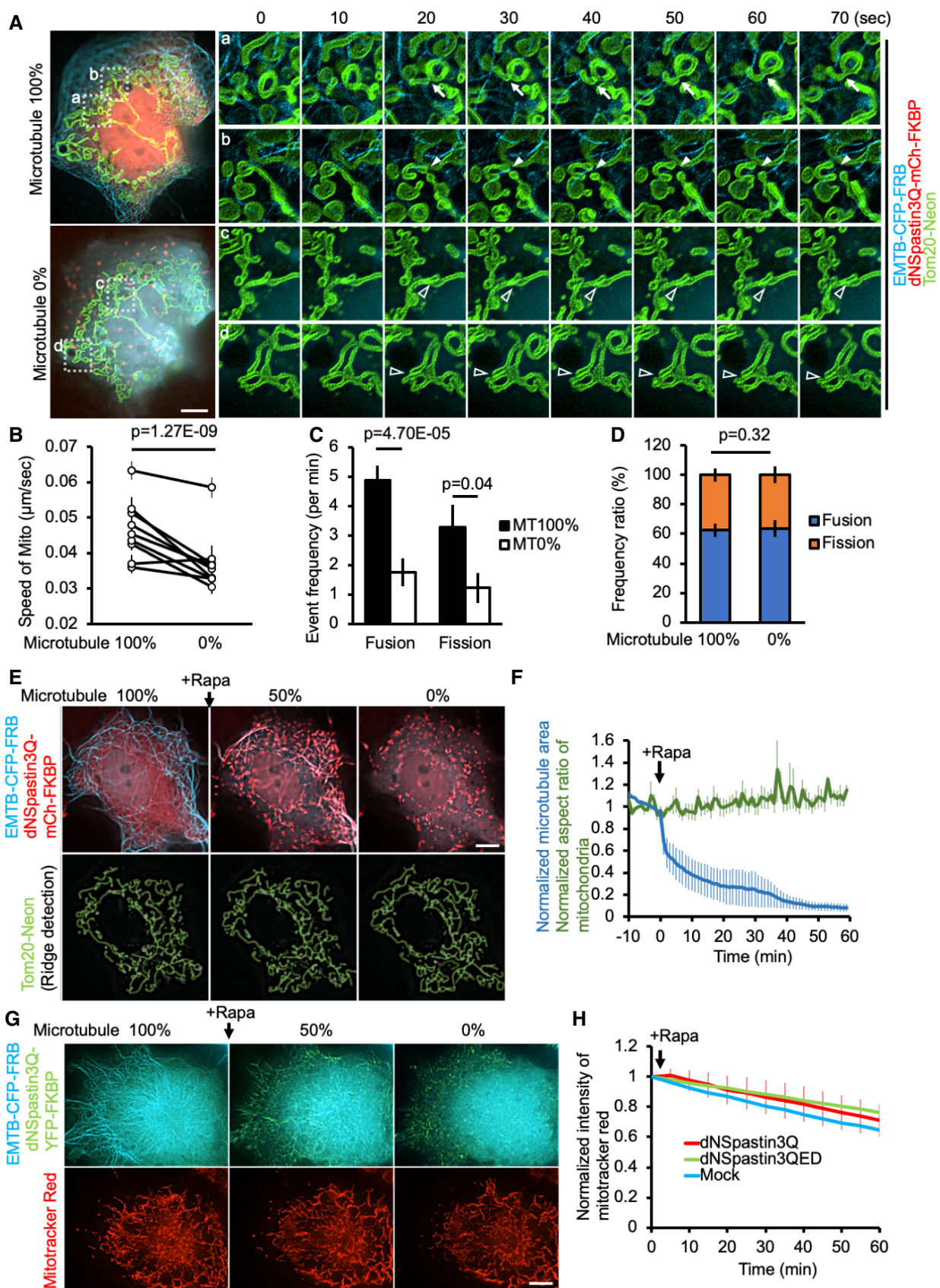


Figure 5.

Figure 5. Effects of acute microtubule disassembly on the dynamics and activities of mitochondria.

- A COS7 cells co-transfected with EMTB-CFP-FRB (blue), dNSpastin3Q-mCh-FKBP (red), and Tom20-Neon (yellow), were treated with rapamycin for acute microtubule disruption. The dynamics of mitochondria at different levels of microtubule disruption are shown. Insets show higher-magnification images of mitochondrial fusion (a, filled arrows), fission (b, filled arrowheads), and unsuccessful fusion (c, d; hollow arrowheads) events as indicated by the dotted squares. Scale bar, 10 μm .
- B Single-cell analysis of local mitochondrial movement before and after microtubule disruption. $n = 6,119$ mitochondria from nine cells, from four independent experiments. Data are shown as the mean \pm SEM.
- C The frequency of mitochondrial fusion and fission events at different levels of microtubule disruption is shown. Data are shown as the mean \pm SEM. $n = 8$ cells from three independent experiments.
- D The ratio of mitochondrial fusion and fission events at different levels of microtubule disruption is shown. Data are shown as the mean \pm SEM. $n = 8$ cells from three independent experiments.
- E, F COS7 cells co-transfected with EMTB-CFP-FRB, dNSpastin3Q-mCh-FKBP, and Tom20-Neon were treated with rapamycin (100 nM) for acute microtubule disruption. The morphology of mitochondria at different levels of microtubule disruption is shown. Scale bar, 10 μm . The ratio of the long axis to the short axis of each mitochondrion and microtubule filament area was determined. $n = 4$ different cells, three independent experiments. Data are shown as the mean \pm SEM.
- G, H The normalized intensity of MitoTracker Red in non-transfected cells (Mock) or cells co-transfected with EMTB-CFRP-FRB and dNSpastin3Q-YFP-FKBP or dNSpastin3QED-YFP-FKBP after rapamycin (Rapa, 100 nM) treatment for the indicated time. Scale bar, 10 μm . $n = 41, 6,$ and 18 cells from three independent experiments. Data are shown as the mean \pm SEM.

Data information: Student's *t*-tests were performed with *P*-values indicated.

Acute microtubule disassembly immediately triggers stress fiber formation and increases cell rigidity

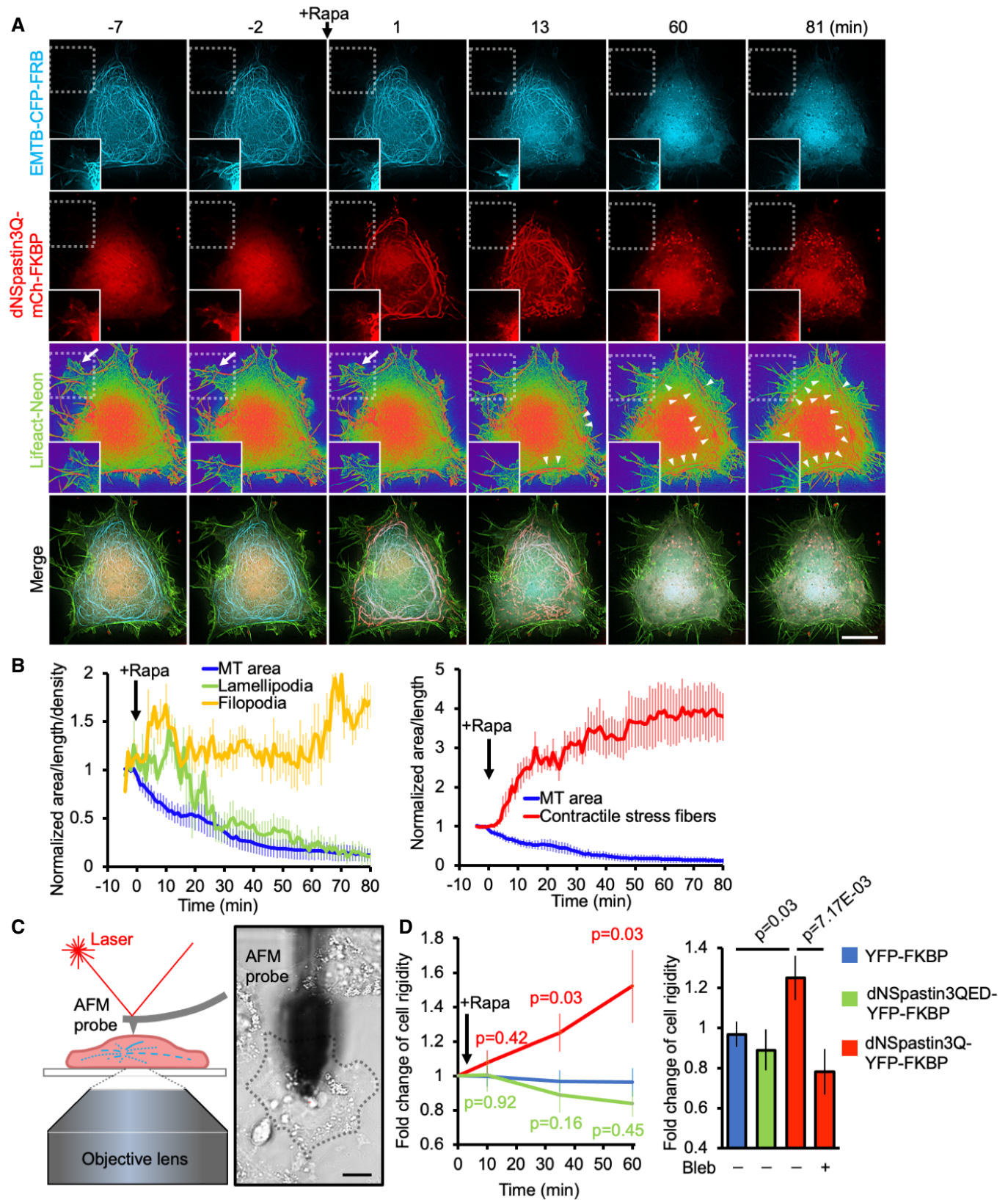
Microtubules crosstalk with actin filaments, especially in many actin-based cell protrusions including lamellipodia and filopodia (Dogterom & Koenderink, 2019; Pimm & Henty-Ridilla, 2021). However, whether microtubule disruption suppresses lamellipodia and/or filopodia formation is still unclear. Taking advantage of the acute disruption of microtubules via our system, we observed the real-time morphology of lamellipodia and filopodia upon microtubule disassembly with a biosensor for actin filaments, Lifeact-Neon. In COS7 cells with intact microtubules, lamellipodia and filopodia were present (Fig 6A and Movie EV30). However, after acute microtubule disruption, only small membrane ruffling, but not large lamellipodia, was observed on the cell periphery (Fig 6A and Movie EV30). The lamellipodia length-to-total plasma membrane ratio was reduced after ~20 min of microtubule disruption (Fig 6B). The quantification data did not show an obvious change in the density of filopodia (the ratio of the number of filopodia to the total plasma membrane length) after the removal of microtubules (Fig 6B). In addition to these actin-based protrusions in the cell periphery, we also noticed that acute microtubule disruption gradually increased the formation of contractile stress fibers in the cell body (Fig 6A and B, Movie EV30). As contractile stress fibers modulate cell rigidity, we therefore observed the fluorescent images of microtubule disruption and characterized the mechanical properties of the imaged cells simultaneously with a hybrid atomic force microscopy (AFM) and confocal microscopy system (Fig 6C) (Kuo et al, 2021). There was a

marked increase in cell rigidity after dNSpastin3Q-triggered microtubule disassembly, which did not occur in the enzyme-dead Spastin and no-Spastin groups (Fig 6D). Upon the treatment of Blebbistatin, an inhibitor of myosin II and contractile stress fiber formation (Dou et al, 2007), Spastin-mediated microtubule disruption could not increase cell rigidity (Fig 6D, right). Taken together, these results indicate that microtubules are important for lamellipodia formation but not for filopodia structures. Microtubules also indirectly modulate cell rigidity by providing support against contractile stress fibers.

There are several possible mechanisms to explain how microtubules play different roles in these actin-based structures. One possible mechanism is that microtubules drive the outward force in cells that is critical for lamellipodia formation but not filopodia formation. A previous characterization of the force exerted by cell protrusions showed that lamellipodia (up to 20 pN) produce forces that are greater than those produced by filopodia (~3 pN). The statement suggesting the development of forces that exceed 3 pN requires microtubules (Cojoc et al, 2007), supports our hypothesis: microtubule-derived force is required for lamellipodia generation in cells. Another possible mechanism is based on a finding, indicating that the formation of lamellipodia, filopodia, and stress fibers is specifically regulated by different small GTPases (Inoue et al, 2005). It is plausible that microtubules modulate corresponding actin-based structures by differentially regulating the signaling of these different small GTPases. Indeed, the microtubule-based promotion of lamellipodia formation via induction of Rac1 small GTPase has been reported (Waterman-Storer et al, 1999). The real-time activities of

Figure 6. Microtubule disassembly enhances stress fiber formation and cell rigidity.

- A COS7 cells co-transfected with EMTB-CFP-FRB (blue), dNSpastin3Q-mCh-FKBP (red), and Lifeact-Neon (heatmap and green) were treated with rapamycin (Rapa, 100 nM) to induce microtubule disassembly. Arrows and arrowheads indicate lamellipodia and stress fibers, respectively. Insets show images of lamellipodia morphology from regions corresponding to the dotted squares with overexposed CFP and mCherry signals. Scale bar, 10 μm .
- B The normalized level of microtubule area, lamellipodia length, and filopodia density of COS7 cells treated as in (A). $n = 4$ cells from three independent experiments. Data are shown as the mean \pm SEM.
- C Schematic representation of the hybrid atomic force microscope and confocal microscope system. A bright-field image of the atomic force microscopy (AFM) probe and an examined cell is shown. Dotted lines indicate the cell boundary. Scale bar, 10 μm .
- D Serial rigidity measurements of COS7 cells that co-expressed EMTB-CFP-FRB and indicated proteins during microtubule disassembly (Left). Blebbistatin (Bleb, 10 μM) was pretreated for 2 h in dNSpastin3Q group and followed by rapamycin treatment for 35 min. The fold change of cell rigidity was then measured by AFM (right). $n = 16, 14, 14,$ and 14 cells in YFP-FKBP, dNSpastin3QED, dNSpastin3Q, and dNSpastin3Q+Bleb groups, respectively, from three independent experiments. Data are shown as the mean \pm SEM. Student's *t*-tests were performed with *P*-values indicated.



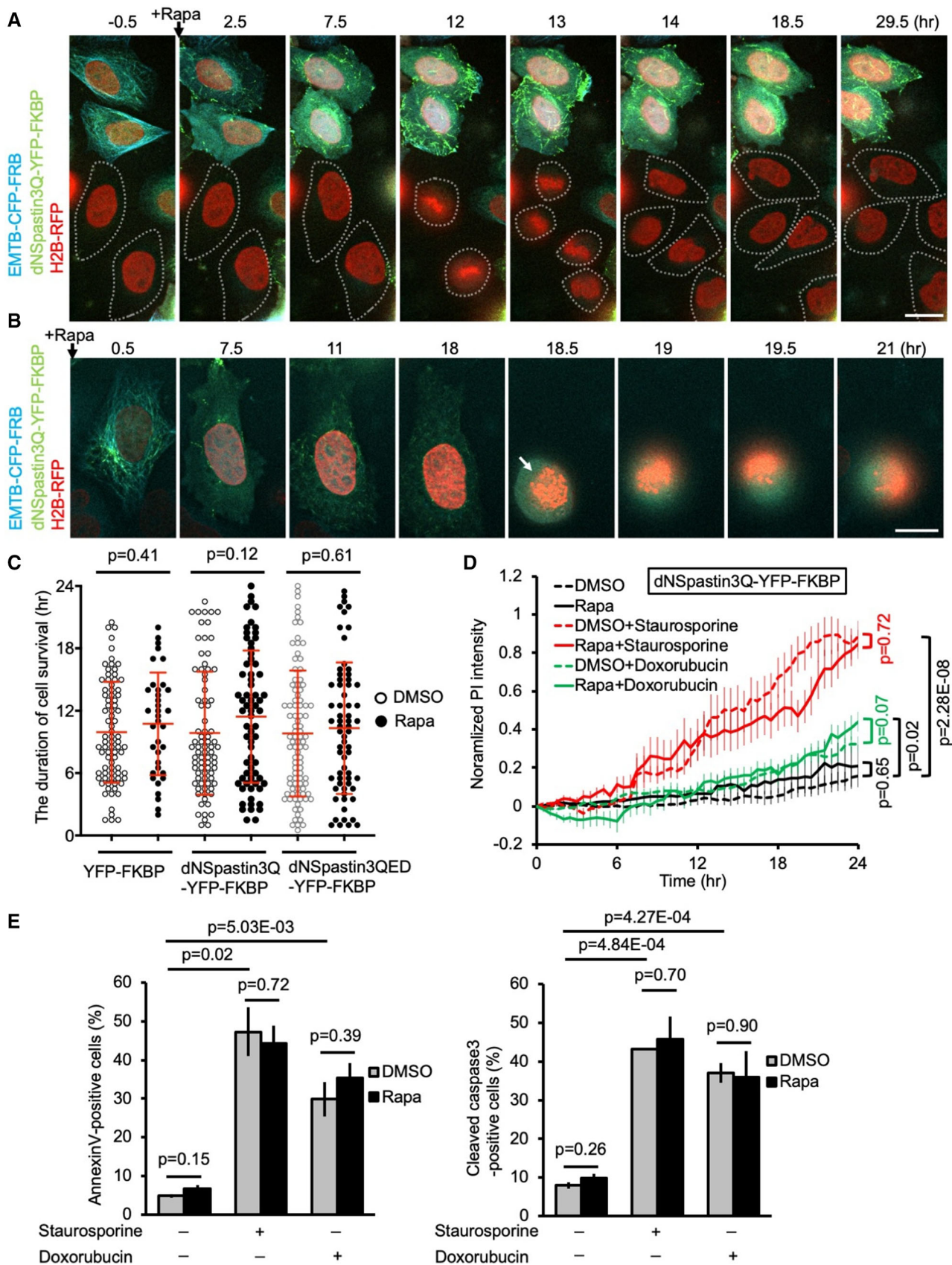


Figure 7.

Figure 7. Microtubule disruption completely prevents cell division and does not lead to cell death in interphase.

- A Unsynchronized HeLa cells were co-transfected with EMTB-CFP-FRB (blue), dNSpastin3Q-YFP-FKBP, and H2B-RFP (a marker of chromosomes, red). After transfection, microtubule disruption was triggered by rapamycin treatment (Rapa, 100 nM) in transfected cells but not in non-transfected cells (highlighted by dotted lines). Scale bar, 10 μ m.
- B An EMTB-CFP-FRB, dNSpastin3Q-YFP-FKBP, and H2B-RFP co-transfected HeLa cell was treated with rapamycin (Rapa, 100 nM) to induce microtubule disruption. Arrows indicate the condensed chromosomes during prophase. Scale bar, 10 μ m.
- C The duration of cell survival in HeLa cells co-transfected with EMTB-CFP-FRB and the indicated constructs upon treatment with 0.1% DMSO (vehicle control) or rapamycin (Rapa, 100 nM) was determined by 30 h time-lapse imaging. $n = 81, 36, 81, 68, 94,$ and 66 cells from left to right, from three independent experiments. Individual data points and the mean \pm SD (red lines) are shown.
- D Unsynchronized HeLa cells were co-transfected with EMTB-CFP-FRB and dNSpastin3Q-YFP-FKBP. At 24 h after transfection, cells were incubated with propidium iodide (PI, 1:250 diluted in culture medium) and treated with 0.1% DMSO or rapamycin (Rapa, 100 nM) with or without staurosporine (50 nM) or doxorubicin (0.3 μ M) for 24 h. The normalized intensity of PI in the transfected cells is shown. $n = 34, 14, 12, 25, 74,$ and 62 cells in the DMSO, Rapa, DMSO+Staurosporine, Rapa+Staurosporine, DMSO+Doxorubicin, and Rapa+Doxorubicin groups, respectively, from three independent experiments. Data are shown as the mean \pm SEM.
- E Unsynchronized HeLa cells co-transfected with EMTB-CFP-FRB and dNSpastin3Q-YFP-FKBP were treated with 0.1%DMSO or rapamycin (Rapa, 100 nM) for 1 h and followed by 24 h of staurosporine (50 nM) or doxorubicin (0.3 μ M) treatment. Treated cells were fixed and stained with Annexin V and cleaved caspase-3 antibody, respectively. The percentage of Annexin V and cleaved caspase-3-positive cells are shown. Data are shown as the mean \pm SEM. $n = 450, 235, 199, 195, 187, 119, 330, 213, 198, 220, 216,$ and 178 cells from left to right, from three independent experiments. Data are shown as the mean \pm SEM.

Data information: Student's t-tests were performed with P -values indicated.

different small GTPases upon acute microtubule disruption merit comprehensive scrutiny to assess this possible mechanism.

Microtubule disruption completely prevents cell division and does not lead to cell death during interphase

Our results demonstrated that microtubule disruption robustly perturbed a wide range of cellular architectures and activities. We next aimed to test whether these defects induced by microtubule disruption lead to cell death. Our chemogenetic system allows for the sustained recruitment of dNSpastin3Q at microtubules, which maintains microtubules in a disassembled state for as long as 30–60 h (Fig 7A and Movie EV31; Appendix Fig S14). Surprisingly, microtubule disassembly in unsynchronized HeLa, COS7, and 293T cells did not shorten the average duration of cell survival as compared to the control conditions (Fig 7A and C, Movie EV31; Appendix Fig S14). After 18 h of persistent microtubule disruption, many cells were arrested in G2/M phase as evidenced by the elevation of a G2/mitotic-specific marker, cyclin B1 level (Appendix Fig S15). A chromosome marker, H2B-RFP, permits the determination of cell cycle stages in live-cell imaging (Fig 7A and B). In the absence of microtubules, none of the cells examined in our experiments could enter mitosis without microtubules (Fig 7B). Control cells with intact microtubules were able to complete cell division (Fig 7A and Movie EV31). In addition to examining cell morphology, we also used a membrane-impermeable DNA dye, propidium iodide (PI), to label dead cells (which do not have intact cell membranes) (Fig 7D). Rapamycin triggered microtubule disruption in dNSpastin3Q-YFP-FKBP and EMTB-CFP-FRB co-transfected cells but did not increase the population of PI-positive cells as compared to the same cells treated with DMSO (Fig 7D). Microtubules are reported to be important for apoptosis signaling (Giannakakou *et al*, 2002; Oropesa-Ávila *et al*, 2013). This raises the possibility that microtubule disruption inactivates apoptotic machinery during interphase, which allows the cells to survive even though they have accumulated many defects. To address this assumption, we tested whether microtubule disruption is able to suppress staurosporine- or doxorubicin-induced apoptosis. As expected, staurosporine and doxorubicin treatments significantly increased the population of PI, Annexin V, and cleaved caspase-3-positive cells with intact

microtubules. However, microtubule disruption did not inhibit staurosporine and doxorubicin-induced apoptosis (Fig 7D and E). In summary, microtubule disruption completely prevented cell division but did not lead to cell death in interphase cells with functional apoptosis machinery.

These results suggest that microtubule disruption does not act as an intrinsic cue to trigger apoptosis in HeLa cells. The spindle assembly checkpoint does, however, seem to be a key mechanism that leads to the death of microtubule-deficient cells, as none of the tested cells enter mitosis (Fig 7B). A high-throughput screen of 15 different cell types that were exposed to different MTAs showed variability in the resulting cell fates under different conditions (Gascoigne & Taylor, 2008), suggesting that what we observed in HeLa cells, COS7 cells, and 293T cells here could be a cell type-specific event. Nevertheless, our system provides a platform with which to study how microtubule disruption determines the fates of quiescent and mitotic cells.

Discussion

We have described here a series of chemogenetic and optogenetic tools that recruit engineered Spastins onto target microtubule subtypes for acute microtubule disassembly in a reversible manner. These tools are able to rapidly disassemble long-lived acetylated microtubules, which are resistant to MTA perturbation (Fig 1F and G). With this capability, the translocation of engineered Spastins onto several acetylated microtubule structures including primary cilia, mitotic spindles, and intercellular bridges (Janke & Magiera, 2020) efficiently disrupted the corresponding structures (Fig 2). In addition to long-lived microtubules, the dynamic microtubules with tyrosination modification can be targeted and disrupted specifically by the combination of a tyrosinated microtubule biosensor and our microtubule disruption system (Fig 3; Kesarwani *et al*, 2020). To our knowledge, this is the first system that permits the rapid disassembly of targeted microtubule subtypes and microtubule-based structures. The swift and complete removal of microtubules enables us to clearly distinguish microtubule-dependent and -independent mechanisms. For instance, microtubules participate in the directed movement of post-Golgi vesicles and lysosomes as well as the

fusion/fission of mitochondria (Figs 5 and EV4, Movies EV20–EV23 and EV27). Intact microtubules maintain the perinuclear distribution of the Golgi and ER tubules (Fig EV5, Movies EV24–EV26). Moreover, microtubules are important for the formation of large lamellipodia and prevent the formation of contractile stress fibers and the resulting increase in cell rigidity (Fig 6 and Movie EV31). We also uncovered several microtubule-independent processes, as microtubules have minimal roles in filopodia formation and in maintaining the mitochondria membrane potential, as well as in the initiation of apoptosis (Figs 5G and H, 6A and B, 7D and E, Movies EV29–EV31).

There are several potential concerns over our system. First, the expression of microtubule-associated proteins such as EMTB may perturb microtubule properties. Indeed, compared with non-transfected cells, there was a marginal increase in microtubule level under the expression of EMTB. However, both nocodazole and colchicine slowly disassembled microtubules in cells with or without EMTB expression, indicating its modest stabilizing effect on microtubules (Appendix Fig S1D). Moreover, our results showed that cells co-expressing EMTB-CFP-FRB and dNSpstin3Q-YFP-FKBP exhibited normal morphology and could properly undergo cell division, suggesting the expression of these components does not induce adverse effects in cells in the absence of protein dimerization (Movie EV32). Second, the expression level of dNSpstin3Q may need to be optimized for low severing background and high disruption effect before and after protein dimerization, respectively. Although variation in microtubule level naturally exists in different cells, microtubules level was 40% higher in most transfected cells than in those non-transfected cells without rapamycin treatment. And, there was no strong correlation between microtubule level and EMTB/dNSpstin3Q level (Fig EV1D, Left). Rapamycin treatment robustly decreased microtubule level in cells expressing either low or high levels of EMTB/dNSpstin3Q (Fig EV1D, Right). In summary, our system efficiently triggers microtubule disruption regardless of the expression level of EMTB/dNSpstin3Q.

Overexpression of unmodified Spastin (SpastinFL) and dNSpstin depleted 47.45% and 42.86% of cytosolic microtubules, respectively (Fig EV1). Spastin-mediated cleavage of microtubules was boosted by recruiting dNSpstin onto microtubules with a 1 h incubation of rapamycin, which removes 74.75% of microtubules (Fig EV1). These results suggest a key role for microtubule association in regulating spastin-mediated microtubule cleaving. Previous *in vitro* and *in vivo* studies have demonstrated that tubulin glutamylation acts as a fine regulator to modulate microtubule binding and cleavage by Spastins, which supports this assumption (Lacroix et al, 2010; Valenstein & Roll-Mecak, 2016). Moreover, PTMs of microtubules may also regulate the severing activity of Spastin. Indeed, our results demonstrated that microtubule hyperglutamylation induced by TLL4C639 overexpression prevents modified microtubules from Spastin-mediated severing (Fig EV3 and Movie EV16). The effects of other PTMs on Spastin-dependent microtubule severing are worthy of comprehensive evaluation.

Spastin is involved in microtubule reorganization (Kuo et al, 2019). For example, Spastin preferentially localizes to axon branching points in neuronal cells to locally destabilize microtubules and facilitate the elongation of branched microtubules (Yu et al, 2008). Our results showed that remnants of digested

microtubules derived from Spastin-mediated severing are able to serve as platforms to extend nascent microtubules when activity and microtubule association of Spastin are inhibited (Figs 4C and EV2, Movies EV9 and EV18). Several microtubule nucleation factors such as SSNA1 localize to axon branching sites and may cooperate with Spastin to initiate branched axons (Basnet et al, 2018). Whether microtubule nucleation factors accumulate on microtubule fragments upon this acute microtubule disassembly needs to be comprehensively evaluated to better understand the molecular mechanisms of Spastin-mediated microtubule remodeling.

The subcellular distribution of Spastin has been well studied, as it is preferentially enriched among cytosolic microtubules, the mitotic spindle, and intercellular bridges (Errico et al, 2004; Yu et al, 2008). Moreover, co-fractionation of Spastin with the centrosome marker γ -tubulin implies that Spastin may also be anchored to centrosomes/basal bodies (Errico et al, 2004), and glutamylation on centrosomes may facilitate Spastin-mediated severing (Lacroix et al, 2010). To test whether Spastin is involved in microtubule severing in different subcellular regions, we recruited Spastin onto specific pools of microtubules. Among all microtubule structures examined, the centrosome was the one resistant to Spastin-mediated microtubule severing (Appendix Fig S12 and Movie EV14). There are three explanations for this phenomenon. First, the unique triplet structure of centrosomal microtubules may contribute to the centrosome's ability to withstand Spastin-mediated severing. The second possibility is that glutamylation on centrioles contributes to their resistance to severing as we found that hyperglutamylation suppresses Spastin's severing (Fig EV3 and Movie EV16). Thirdly, the anchoring orientation of EMTB-CFP-FRB may not allow the Spastin-mediated severing reaction at centrosomes. Experiments evaluating the effect of Spastin on centrosomes that lack microtubule triplets (Wang et al, 2017) or glutamylation and that use different centrosomal-targeting proteins will be useful for addressing these possible mechanisms.

To precisely control microtubule properties, many photoswitchable MTAs have been developed to manipulate microtubules under the control of light illumination (Borowiak et al, 2015; Müller-Deku et al, 2020). These chemicals can be easily introduced into target cells without genetic modification. However, thus far, the photoswitchable MTAs against specific microtubule subtypes are still sparse. In contrast, our genetically encoded system can be driven by tissue-specific promoters. Together with microtubule subtype-specific biosensors or associated proteins (Hong et al, 2018; Kesarwani et al, 2020), our approaches are promising to precisely perturb specific microtubule subpopulations in target cells *in vitro* and *in vivo*.

In summary, we here provide proof-of-concept approaches to disrupt target microtubule subtypes, which open new avenues to understand the functions of different tubulin isoforms and tubulin PTMs. Our system also provides insights into how Spastin modulates microtubule severing and serves as a powerful tool for distinguishing microtubule-dependent and microtubule-independent mechanisms and for dissecting causal relationships between microtubules of interest and cellular events. This precise microtubule manipulation system represents a fundamental step in developing new strategies to treat various diseases such as tumors and neurodegeneration and developmental disorders in which microtubule-mediated events have gone awry.

Materials and Methods

Cell culture and transfection

COS7, HeLa, U2OS, HEK293T, and NIH3T3 cells were maintained at 37°C, 5% CO₂, and 95% humidity in Dulbecco's modified Eagle's medium (DMEM) supplemented with 10% fetal bovine serum (FBS), and penicillin and streptomycin (Corning). To induce ciliogenesis, NIH3T3 cells were serum-starved for 24 h. COS7 cells were transfected with plasmid DNAs by using TurboFect transfection reagents (Thermo Fisher). HeLa, U2OS, HEK293T, and NIH3T3 cells were transfected with FuGENE HD (Promega). Transfected cells were incubated for 24–48 h prior to imaging and other experiments.

DNA constructs

We obtained constructs encoding the most abundantly expressed isoform of Spastin in cells (58 kDa; starting at position M85 in the mouse Spastin sequence), a truncated form of dNSpastin that is missing the N-terminal 1–140 amino acids (the shortest active truncated version of Spastin), and the enzyme-inactive versions SpastinFLED and dNSpastinED, each of which was tagged with EYFP (SpastinFL-YFP, dNSpastin-YFP, SpastinFLED-YFP, and dNSpastinED-YFP), from Dr. Carsten Janke (Institut Curie). To remove the microtubule-binding domain of dNSpastin, the catalytic AAA domain of dNSpastin (dNSpstinCD) was amplified by PCR-based methods. Three residues of Spastin were mutated to QQQ (dNSpastin3Q) by site-directed mutagenesis DNA encoding individual forms of dNSpastin (dNSpastin, dNSpastinED, dNSpastinCD, and dNSpastin3Q) was then cloned into the YFP-FKBP vector (pEGFP-C1 backbone) to generate dNSpastin-YFP-FKBP, dNSpastinCD-YFP-FKBP, and dNSpastin3Q-YFP-FKBP. Using this method, we also generated the enzyme-inactive dNSpastin3QED-YFP-FKBP construct. dNSpastin-YFP-FKBP-C2Lact was generated by inserting the C2Lact sequence between the HindIII and BamHI restriction sites in dNSpastin-YFP-FKBP. The DNA fragments of A1AY1, TagRFP, and TagCFP were synthesized with codon optimization and subcloned to FRB and FKBP vectors. We transformed each construct into competent cells and isolated single clones for DNA purification. All DNA constructs were verified by DNA sequencing. The detailed protein sequences of constructs used in this study are provided in [Appendix](#) protein sequence.

Immunofluorescence staining

Cells cultured in borosilicate glass Lab-Tek eight-well chambers (Nunc) were fixed in 4% paraformaldehyde (Electron Microscopy Sciences) at room temperature for 15 min. Fixed cells were permeabilized with 0.1% Triton X-100 and then incubated in blocking solution (phosphate-buffered saline with 2% bovine serum albumin) for 30 min at room temperature. To label cytosolic microtubules, primary ciliary membrane, and axonemal microtubules, cells were incubated for 1 h at room temperature with mouse antibody against α -tubulin (1:500; Sigma Aldrich, T6199), rabbit antibody against Arl13b (1:500; Proteintech, 17711-1-AP), mouse antibody against glutamylated tubulin (1:100; Adipogen, AG-20B-0020-C100), mouse antibody against acetylated tubulin (1:500; Sigma Aldrich, T7451), rat antibody against tyrosinated tubulin

(1:100; Sigma Aldrich, MAB1864), rabbit antibody against cyclin B1 (1:500; Genetex, GTX100911), and mouse antibody against detyrosinated tubulin (1:100; MERCK, AB3201) each of which was diluted in blocking solution. Cells were then washed with PBS and incubated for 1 h with appropriate secondary antibodies (1:1,000 dilution; Thermo Fisher) at room temperature.

Western blotting

HEK293T cells were co-transfected with EMTB-CFP-FRB and YFP-FKBP, dNSpastin3Q-YFP-FKBP, or dNSpastin3QED-YFP-FKBP. Two days after transfection, cells were incubated with 50 μ M MG132 (Sigma Aldrich) for 30 min and then treated with 100 nM rapamycin or 0.1% DMSO (vehicle control) for 30 min prior to cell collection. For the cold treatment (4°C), untransfected HEK293T cells were put on ice for 40 min to depolymerize microtubules. Cells were lysed in RIPA lysis buffer (50 mM Tris-HCl, pH 7.6; 2 mM EGTA; 9% NaCl; 1% Triton X-100) containing protease inhibitors (Roche). Protein concentrations were measured with the Bio-Rad Protein Assay. Cell lysates were diluted with 2 \times Laemmli sample buffer (Bio-Rad) and boiled at 95°C for 10 min and then underwent western blotting. After the transfer process, the PVDF membranes (Bio-Rad) were incubated with blocking buffer (5% skim milk in Tris-buffered saline with Tween 20; TBST) for 1 h at room temperature and then stained with primary antibodies against α -tubulin (1:1,000; Sigma Aldrich, T6199) and GAPDH (1:5,000; Cell Signaling, 2118), which were diluted with blocking buffer, overnight at 4°C. Membranes were washed with TBST and then were incubated with horseradish peroxidase-conjugated secondary antibodies diluted in blocking buffer (anti-rabbit, 1:10,000; anti-mouse, 1:5,000) for 1 h at room temperature. The bioluminescence signal was detected with AmershamTM ECL SelectTM (GE Healthcare), and blot images were acquired with an iBrightTM FL1500 Instrument (Thermo Fisher).

Live-cell imaging

Live transfected cells cultured on poly(D-lysine)-coated glass coverslips (Hecht Assistant) were treated with either 100 nM rapamycin for rapid induction of protein dimerization and translocation or microtubule-targeting agents (3.3 μ M nocodazole or 500 μ M colchicine) during imaging. Live-cell imaging was conducted on a Nikon T1 inverted fluorescence microscope (Nikon) with a 60 \times oil objective (Nikon), a Prime camera (Photometrics), and 37°C, 5% CO₂ heat stage (Live Cell Instrument). Rapid recruitment of POIs was imaged at 5- or 10-s intervals, whereas the process of microtubule disruption was imaged at 1-min intervals. Images were obtained using Nikon NIS-Elements AR software and processed with Huygens Deconvolution Software (Scientific Volume Imaging). Image analysis was mainly performed with Nikon NIS-Elements AR software.

Photostimulation

COS7 cells were plated on poly(D-lysine)-coated coverslips and cultured in six-well plates (Thermo Scientific) for 48 h. Before imaging, cells were incubated with SPY650-tubulin (1,000-fold dilution; Spirochrome) at 37°C for 1 h. Local photostimulation was carried out with a fluorescence microscope (Nikon) equipped with a digital

micromirror device, polygon 400 (MIGHTEX), and a 488-nm light source. Cells were illuminated with the blue light (5 s on/1 s off; 1.6 nW/ μm^2) for the indicated duration. The mCherry and SPY650-tubulin were simultaneously imaged during photostimulation using Nikon element AR software.

Measurement of microtubule filament area

The microtubule filaments in living cells were labeled with EMTB-CFP-FRB and imaged in real-time (RAW image). The rolling ball correction was used to remove the cytosol background from the RAW images, which was carried out with the Nikon NIS-Elements AR software. Images were processed to generate the binary microtubule filament pattern via the Otsu threshold and analyzed by Fiji software (Appendix Fig S16).

Tracking vesicles and lysosomes

Cos7 cells co-transfected with plasmids encoding LAMP3-YFP or TGN38-YFP were imaged for 20 min with an interval of 30 s. To obtain the trajectories of LAMP3/TGN38-positive vesicles, recorded data were analyzed with Fiji software with a plugin, trackmate. The trajectory data were then processed by Moment Scaling Spectrum analysis (software is available at <https://www.utsouthwestern.edu/labs/jaqaman/software/>). According to their movement patterns, the LAMP3/TGN39-positive puncta were classified as confined movement, free diffusion, and directed diffusion. The displacement and velocity of LAMP3-YFP/TGN38-YFP were tracked and analyzed by the DoG detector and Simple LAP tracker in the Fiji software plugin Trackmate. Estimated blob diameter was set at 0.8–1 μm , linking max distance at 2 μm , gap-closing distance at 2 μm , and gap-closing max frame gap at 0.

Analysis of mitochondrial morphology and dynamics

Cos7 cells co-transfected with plasmids encoding Tom20-Neon, dNSpstin3Q-mCherry-FKBP, and EMTB-CFP-FRB were imaged at 1-min intervals and treated with 100 nM rapamycin during imaging. In this study, we used a series of ImageJ tools for mitochondrial network morphology analysis (Valente *et al*, 2017) to measure the aspect ratio of mitochondria in live cells. Images were first pre-processed to obtain sharper and higher contrast for better analysis by applying “unsharp mask” filtering, “enhance local contrast (CLAHE),” and median filtering in ImageJ. Mitochondrial length and width were then estimated by the ImageJ plugin “Ridge Detection” to obtain the aspect ratio of the mitochondria.

To analyze mitochondrial dynamics, transfected Cos7 cells were imaged at 10-s intervals for 5 min before and 30 min after 100 nM rapamycin treatment. The live-cell images were then analyzed with the MATLAB GUI Mitometer app to automatically track and estimate the speed of mitochondrial movement (Lefebvre *et al*, 2021).

Force measurements using atomic force microscopy

Force measurements were performed with the co-axis system for confocal microscopy (FV3000, Olympus Corporation) and atomic force microscopy (BioScope Resolve, Bruker Corporation) as described (Kuo *et al*, 2021). Before measurements were made, the

deflection sensitivity and spring constant of the atomic force microscopy probe (PFQNM-LC-A-CAL, Bruker Corporation) were adjusted with the No-Touch calibration mode. Briefly, living COS7 cells with microtubule disassembly and control COS7 cells were cultured in DEME with 10% FBS and located by confocal microscopy. The rigidity of the selected cell was measured with the Fast-Force Volume mode at the indicated time point through atomic force microscopy. Then, cell rigidity was calculated from force-distance curves that were fit to the Sneddon model through NanoScope Analysis. Cell rigidity at different time points was normalized to the original rigidity of that cell. In the contractile stress fiber inhibition experiment, transfected cells were pretreated with Blebbistatin (10 μM ; Sigma Aldrich) for 2 h before AFM measurement.

Cell synchronization

In the experiments of Fig 2C and E, Appendix Fig S9C and E, plasmid DNA transfection was carried out 20–24 h prior to cell cycle synchronization. For synchronization, HeLa cells were treated with 2 mM thymidine (Sigma) for 16–18 h to induce arrest at G1/S phase and then were treated with 2.5 ng/ml RO3306 (Sigma) for 12 h to induce arrest at G2/M phase. After being washed with warm DMEM, cells were incubated with DMEM and 10% FBS at 37°C, 5% CO₂ for 30–60 min to enrich the population of metaphase and telophase cells.

Statistical analysis

We first determined whether variances were equal or not with the F-test and then used the unpaired two-tailed Student's *t*-test to calculate *P*-values via PRISM 6 software. A *P*-value of < 0.05 indicated a significant difference, and *P* < 0.01 indicated a highly significant difference.

Data availability

This study does not contain data amendable to external repositories.

Expanded View for this article is available online.

Acknowledgements

We thank Dr. Carsten Janke (Institut Curie) for the Spstin and TTL4 constructs. This study was supported by the Ministry of Science and Technology (MOST), Taiwan (MOST grant numbers 110-2636-B-007-011 and 111-2636-B-007-009 to Y.C.L. A1101-0607 to M.J.T.), and Ministry of Education (MOE), Taiwan (MOE grant number D110-H4001 to M.J.T.). National Tsing Hua University (grant number 111Q2713E1 to Y.C.L.)

Author contributions

Grace Y Liu: Data curation; Software; Formal analysis; Validation; Investigation; Visualization; Methodology; Writing—original draft. **Shiau-Chi Chen:** Formal analysis; Validation; Investigation; Visualization; Methodology. **Gang-Hui Lee:** Formal analysis; Validation; Investigation; Visualization. **Kritika Shaiv:** Formal analysis; Investigation; Visualization; Methodology. **Pin-Yu Chen:** Formal analysis; Validation; Investigation; Visualization; Methodology. **Hsuan Cheng:** Software; Supervision; Validation; Methodology. **Shi-Rong Hong:** Formal analysis; Investigation; Visualization; Methodology. **Wen-Ting**

Yang: Formal analysis; Validation; Investigation; Visualization; Methodology. **Shih-Han Huang:** Investigation; Methodology. **Ya-Chu Chang:** Investigation; Methodology. **Hsien-Chu Wang:** Investigation; Methodology. **Ching-Lin Kao:** Validation; Investigation; Methodology. **Pin-Chiao Sun:** Investigation; Methodology. **Ming-Hong Chao:** Investigation. **Yian-Ying Lee:** Investigation. **Ming-Jer Tang:** Supervision; Funding acquisition; Methodology. **Yu-Chun Lin:** Resources; Software; Formal analysis; Supervision; Funding acquisition; Validation; Investigation; Visualization; Methodology; Writing—original draft; Project administration; Writing—review & editing.

In addition to the CRediT author contributions listed above, the contributions in detail are:

GYL, KS, and Y-CL designed and conducted the experiments. GYL, S-CC, KS, and Y-CC generated DNA constructs. S-RH performed western blotting analysis. S-CC, W-TY, and Y-CC conducted the photostimulation experiments. C-LK and HC analyzed the dynamics of vesicles and lysosomes. GYL, H-CW, P-CS, M-HC, Y-YL, and Y-CL analyzed imaging data. S-HH conducted cell synchronization. P-YC conducted the cell apoptosis experiments. G-HL and HC performed cell force measurement under the supervision of M-JT. Y-CL, GYL, G-HL, and W-TY wrote the manuscript.

Disclosure and competing interests statement

The patent for acute microtubule disassembly developed in this study is pending.

References

- Adikes RC, Hallett RA, Saway BF, Kuhlman B, Slep KC (2018) Control of microtubule dynamics using an optogenetic microtubule plus end-F-actin cross-linker. *J Cell Biol* 217: 779–793
- Aillaud C, Bosc C, Peris L, Bosson A, Heemeryck P, Van Dijk J, Le Fric J, Boulan B, Vossier F, Sanman LE et al (2017) Vasohibins/SVBP are tubulin carboxypeptidases (TCPs) that regulate neuron differentiation. *Science* 358: 1448–1453
- Antanavičiūtė I, Gibieža P, Prekeris R, Skeberdis VA (2018) Midbody: from the regulator of cytokinesis to postmitotic signaling organelle. *Med* 54: 1–10
- Ba Q, Raghavan G, Kiselyov K, Yang G (2018) Whole-cell scale dynamic organization of lysosomes revealed by spatial statistical analysis. *Cell Rep* 23: 3591–3606
- Bannai H, Inoue T, Nakayama T, Hattori M, Mikoshiba K (2004) Kinesin dependent, rapid, bi-directional transport of ER sub-compartment in dendrites of hippocampal neurons. *J Cell Sci* 117: 163–175
- Basnet N, Nedožralova H, Crevenna AH, Bodakuntla S, Schlichthaerle T, Taschner M, Cardone G, Janke C, Jungmann R, Magiera MM et al (2018) Direct induction of microtubule branching by microtubule nucleation factor SSNA1. *Nat Cell Biol* 20: 1172–1180
- Bates D, Eastman A (2017) Microtubule destabilising agents: far more than just antimetabolic anticancer drugs. *Br J Clin Pharmacol* 83: 255–268
- Borowiak M, Nahaboo W, Reynders M, Nekolla K, Jalinot P, Hasserodt J, Rehberg M, Delattre M, Zahler S, Vollmar A et al (2015) Photoswitchable inhibitors of microtubule dynamics optically control mitosis and cell death. *Cell* 162: 403–411
- Cleary JM, Hancock WO (2021) Molecular mechanisms underlying microtubule growth dynamics. *Curr Biol* 31: R560–R573
- Cojoc D, Difato F, Ferrari E, Shahapure RB, Laishram J, Righi M, Di Fabrizio EM, Torre V (2007) Properties of the force exerted by filopodia and lamellipodia and the involvement of cytoskeletal components. *PLoS One* 2: e1072
- Csordás G, Várnai P, Golenár T, Roy S, Purkins G, Schneider TG, Balla T, Hajnóczky G (2010) Imaging interorganelle contacts and local calcium dynamics at the ER-mitochondrial interface. *Mol Cell* 39: 121–132
- Cupido T, Pisa R, Kelley ME, Kapoor TM (2019) Designing a chemical inhibitor for the AAA protein spastin using active site mutations. *Nat Chem Biol* 15: 444–452
- DeRose R, Miyamoto T, Inoue T (2013) Manipulating signaling at will: chemically-inducible dimerization (CID) techniques resolve problems in cell biology. *Pflugers Arch* 465: 409–417
- van Dijk J, Rogowski K, Miro J, Lacroix B, Eddé B, Janke C (2007) A targeted multienzyme mechanism for selective microtubule polyglutamylation. *Mol Cell* 26: 437–448
- Dogterom M, Koenderink GH (2019) Actin–microtubule crosstalk in cell biology. *Nat Rev Mol Cell Biol* 20: 38–54
- Dou Y, Arlock P, Arner A (2007) Blebbistatin specifically inhibits actin-myosin interaction in mouse cardiac muscle. *Am J Physiol Cell Physiol* 293: C1148–C1153
- Doxsey S, McCollum D, Theurkauf W (2005) Centrosomes in cellular regulation. *Annu Rev Cell Dev Biol* 21: 411–434
- Eckert T, Le DT, Link S, Friedmann L, Woehlke G (2012) Spastin's microtubule-binding properties and comparison to katanin. *PLoS One* 7: e50161
- Errico A, Claudiani P, D'Addio M, Rugarli EI (2004) Spastin interacts with the centrosomal protein NA14, and is enriched in the spindle pole, the midbody and the distal axon. *Hum Mol Genet* 13: 2121–2132
- Fan C-H, Huang Y-S, Huang W-E, Lee AA, Ho S-Y, Kao Y-L, Wang C-L, Lian Y-L, Ueno T, Andrew Wang T-S et al (2017) Manipulating cellular activities using an ultrasound-chemical hybrid tool. *ACS Synth Biol* 6: 2021–2027
- Friedman JR, Webster BM, Mastronarde DN, Verhey KJ, Voeltz GK (2010) ER sliding dynamics and ER-mitochondrial contacts occur on acetylated microtubules. *J Cell Biol* 190: 363–375
- Gascoigne KE, Taylor SS (2008) Cancer cells display profound intra- and interline variation following prolonged exposure to antimetabolic drugs. *Cancer Cell* 14: 111–122
- Giannakakou P, Nakano M, Nicolaou KC, O'Brate A, Yu J, Blagosklonny MV, Greber UF, Fojo T (2002) Enhanced microtubule-dependent trafficking and p53 nuclear accumulation by suppression of microtubule dynamics. *Proc Natl Acad Sci USA* 99: 10855–10860
- Gillingham AK, Munro S (2000) The PACT domain, a conserved centrosomal targeting motif in the coiled-coil proteins AKAP450 and pericentrin. *EMBO Rep* 1: 524–529
- Guo Y, Li DI, Zhang S, Yang Y, Liu J-J, Wang X, Liu C, Milkie DE, Moore RP, Tulu US et al (2018) Visualizing intracellular organelle and cytoskeletal interactions at nanoscale resolution on millisecond timescales. *Cell* 175: 1430–1442
- Hildebrandt F, Benzing T, Katsanis N (2011) Ciliopathies. *N Engl J Med* 364: 1533–1543
- Hong S-R, Wang C-L, Huang Y-S, Chang Y-C, Chang Y-C, Pusapati GV, Lin C-Y, Hsu N, Cheng H-C, Chiang Y-C et al (2018) Spatiotemporal manipulation of ciliary glutamylation reveals its roles in intraciliary trafficking and Hedgehog signaling. *Nat Commun* 9: 1–13
- Huby RD, Weiss A, Ley SC (1998) Nocodazole inhibits signal transduction by the T cell antigen receptor. *J Biol Chem* 273: 12024–12031
- Inoue T, Heo WD, Grimley JS, Wandless TJ, Meyer T (2005) An inducible translocation strategy to rapidly activate and inhibit small GTPase signaling pathways. *Nat Methods* 2: 415–418
- Janke C, Magiera MM (2020) The tubulin code and its role in controlling microtubule properties and functions. *Nat Rev Mol Cell Biol* 21: 307–326

- Jaqaman K, Loerke D, Mettlen M, Kuwata H, Grinstein S, Schmid SL, Danuser G (2008) Robust single-particle tracking in live-cell time-lapse sequences. *Nat Methods* 5: 695–702
- Kesarwani S, Lama P, Chandra A, Reddy PP, Jijumon AS, Bodakuntla S, Rao BM, Janke C, Das R, Sirajuddin M (2020) Genetically encoded live-cell sensor for tyrosinated microtubules. *J Cell Biol* 219: e201912107
- Kuo CH, Huang YH, Chen PK, Lee GH, Tang MJ, Conway EM, Shi GY, Wu HL (2021) VEGF-induced endothelial podosomes via ROCK2-dependent thrombospondin expression initiate sprouting angiogenesis. *Arterioscler Thromb Vasc Biol* 41: 1657–1671
- Kuo YW, Trotter O, Mahamdeh M, Howard J (2019) Spastin is a dual-function enzyme that severs microtubules and promotes their regrowth to increase the number and mass of microtubules. *Proc Natl Acad Sci USA* 116: 5533–5541
- Lacroix B, Van Dijk J, Gold ND, Guizetti J, Aldrian-Herrada G, Rogowski K, Gerlich DW, Janke C (2010) Tubulin polyglutamylation stimulates spastin-mediated microtubule severing. *J Cell Biol* 189: 945–954
- LeDizet M, Piperno G (1986) Cytoplasmic microtubules containing acetylated α -tubulin in *Chlamydomonas reinhardtii*: Spatial arrangement and properties. *J Cell Biol* 103: 13–22
- Lefebvre AEY, Ma D, Kessenbrock K, Lawson DA, Digman MA (2021) Automated segmentation and tracking of mitochondria in live-cell time-lapse images. *Nat Methods* 18: 1091–1102
- Lin YC, Nihongaki Y, Liu TY, Razavi S, Sato M, Inoue T (2013) Rapidly reversible manipulation of molecular activity with dual chemical dimerizers. *Angew Chem Int Ed Engl* 52: 6450–6454
- Lu L, Ladinsky MS, Kirchhausen T (2009) Cisternal organization of the endoplasmic reticulum during mitosis. *Mol Biol Cell* 20: 3471–3480
- Meiring JCM, Shneyer BI, Akhmanova A (2020) Generation and regulation of microtubule network asymmetry to drive cell polarity. *Curr Opin Cell Biol* 62: 86–95
- Molero JC, Whitehead JP, Meerloo T, James DE (2001) Nocodazole inhibits insulin-stimulated glucose transport in 3T3-L1 adipocytes via a microtubule-independent mechanism. *J Biol Chem* 276: 43829–43835
- Müller-Deku A, Meiring JCM, Loy K, Kraus Y, Heise C, Bingham R, Jansen KI, Qu X, Bartolini F, Kapitein LC et al (2020) Photoswitchable paclitaxel-based microtubule stabilisers allow optical control over the microtubule cytoskeleton. *Nat Commun* 11: 4640
- Murota Y, Tabu K, Taga T (2016) Requirement of ABC transporter inhibition and Hoechst 33342 dye deprivation for the assessment of side population-defined C6 glioma stem cell metabolism using fluorescent probes. *BMC Cancer* 16: 1–7
- Noordstra I, Akhmanova A (2017) Linking cortical microtubule attachment and exocytosis. *F1000Res* 6: 1–12
- Oropesa-Ávila M, Fernández-Vega A, de la Mata M, Maraver JG, Cordero MD, Cotán D, de Miguel M, Calero CP, Paz MV, Pavón AD et al (2013) Apoptotic microtubules delimit an active caspase free area in the cellular cortex during the execution phase of apoptosis. *Cell Death Dis* 4: 1–13
- Parker AL, Kavallaris M, McCarroll JA (2014) Microtubules and their role in cellular stress in cancer. *Front Oncol* 4: 1–19
- Pimm ML, Henty-Ridilla JL (2021) New twists in actin-microtubule interactions. *Mol Biol Cell* 32: 211–217
- Poteryaev D, Squirrell JM, Campbell JM, White JG, Spang A (2005) Involvement of the actin cytoskeleton and homotypic membrane fusion in ER dynamics in *Caenorhabditis elegans*. *Mol Biol Cell* 16: 2139–2153
- Prosser SL, Pelletier L (2017) Mitotic spindle assembly in animal cells: a fine balancing act. *Nat Rev Mol Cell Biol* 18: 187–201
- Putyrski M, Schultz C (2012) Protein translocation as a tool: the current rapamycin story. *FEBS Lett* 586: 2097–2105
- Rodrigues TB, Ballesteros P (2007) Spastin and microtubules: functions in health and disease. *J Neurosci Res* 3253: 3244–3253
- Rovini A, Savry A, Braguer D, Carré M (2011) Microtubule-targeted agents: when mitochondria become essential to chemotherapy. *Biochim Biophys Acta* 1807: 679–688
- Schroeder LK, Barentine AES, Merta H, Schweighofer S, Zhang Y, Baddeley D, Bewersdorf J, Bahmanyar S (2019) Dynamic nanoscale morphology of the ER surveyed by STED microscopy. *J Cell Biol* 218: 83–96
- Schuh M (2011) An actin-dependent mechanism for long-range vesicle transport. *Nat Cell Biol* 13: 1431–1436
- Schwarz TL (2013) Mitochondrial trafficking in neurons. *Cold Spring Harb Perspect Med* 3: 1–16
- Sferra A, Nicita F, Bertini E (2020) Microtubule dysfunction: a common feature of neurodegenerative diseases. *Int J Mol Sci* 21: 1–36
- Shibata Y, Hu J, Kozlov MM, Rapoport TA (2009) Mechanisms shaping the membranes of cellular organelles. *Annu Rev Cell Dev Biol* 25: 329–354
- Steinmetz MO, Prota AE (2018) Microtubule-targeting agents: strategies to hijack the cytoskeleton. *Trends Cell Biol* 28: 776–792
- Taslimi A, Zoltowski B, Miranda JG, Pathak GP, Hughes RM, Tucker CL (2016) Optimized second generation CRY2/CIB dimerizers and photoactivatable Cre recombinase. *Nat Chem Biol* 12: 425–430
- Terasaki M, Chen LB, Fujiwara K (1986) Microtubules and the endoplasmic reticulum are highly interdependent structures. *J Cell Biol* 103: 1557–1568
- Valenstein ML, Roll-Mecak A (2016) Graded control of microtubule severing by tubulin glutamylation. *Cell* 164: 911–921
- Valente AJ, Maddalena LA, Robb EL, Moradi F, Stuart JA (2017) A simple ImageJ macro tool for analyzing mitochondrial network morphology in mammalian cell culture. *Acta Histochem* 119: 315–326
- Van Haren J, Charafeddine RA, Ettinger A, Wang H, Hahn KM, Wittmann T (2018) Local control of intracellular microtubule dynamics by EB1 photodissociation. *Nat Cell Biol* 20: 252–261
- Voß S, Klewer L, Wu YW (2015) Chemically induced dimerization: reversible and spatiotemporal control of protein function in cells. *Curr Opin Chem Biol* 28: 194–201
- Wang JT, Kong D, Hoerner CR, Loncarek J, Stearns T (2017) Centriole triplet microtubules are required for stable centriole formation and inheritance in human cells. *Elife* 110: 1–17
- Waterman-Storer CM, Worthylake RA, Liu BP, Burdridge K, Salmon ED (1999) Microtubule growth activates Rac1 to promote lamellipodial protrusion in fibroblasts. *Nat Cell Biol* 1: 45–50
- Westermann B (2010) Mitochondrial fusion and fission in cell life and death. *Nat Rev Mol Cell Biol* 11: 872–884
- White SR, Evans KJ, Lary J, Cole JL, Lauring B (2007) Recognition of C-terminal amino acids in tubulin by pore loops in Spastin is important for microtubule severing. *J Cell Biol* 176: 995–1005
- Xie R, Nguyen S, McKeenan WL, Liu L (2010) Acetylated microtubules are required for fusion of autophagosomes with lysosomes. *BMC Cell Biol* 11: 89
- Xu Z, Schaedel L, Portran D, Aguilar A, Gaillard J, Peter Marinkovich M, Théry M, Nachury MV (2017) Microtubules acquire resistance from mechanical breakage through intraluminal acetylation. *Science* 356: 328–332
- Yang WT, Hong SR, He K, Ling K, Shaiv K, Hu JH, Lin YC (2021) The emerging roles of axonemal glutamylation in regulation of cilia architecture and functions. *Front Cell Dev Biol* 9: 622302

Yu W, Qiang L, Solowska JM, Karabay A, Korulu S, Baas PW (2008) The microtubule-severing proteins spastin and katanin participate differently in the formation of axonal branches. *Mol Biol Cell* 19: 1485–1498

Zheng P, Chen Q, Tian X, Qian N, Chai P, Liu B, Hu J, Blackstone C, Zhu D, Teng J et al (2018) DNA damage triggers tubular endoplasmic reticulum extension to promote apoptosis by facilitating ER-mitochondria signaling. *Cell Res* 28: 833–854



License: This is an open access article under the terms of the Creative Commons Attribution-NonCommercial-NoDerivs 4.0 License, which permits use and distribution in any medium, provided the original work is properly cited, the use is non-commercial and no modifications or adaptations are made.